Estimates of Surface Wind Stress and Drag Coefficients in Typhoon Megi

JE-YUAN HSU, REN-CHIEH LIEN, ERIC A. D'ASARO, AND THOMAS B. SANFORD

Applied Physics Laboratory and School of Oceanography, University of Washington, Seattle, Washington

(Manuscript received 22 March 2016, in final form 12 January 2017)

ABSTRACT

Estimates of drag coefficients beneath Typhoon Megi (2010) are calculated from roughly hourly velocity profiles of three EM-APEX floats, air launched ahead of the storm, and from air-deployed dropsondes measurements and microwave estimates of the 10-m wind field. The profiles are corrected to minimize contributions from tides and low-frequency motions and thus isolate the current induced by Typhoon Megi. Surface wind stress is computed from the linear momentum budget in the upper 150 m. Three-dimensional numerical simulations of the oceanic response to Typhoon Megi indicate that with small corrections, the linear momentum budget is accurate to 15% before the passage of the eye but cannot be applied reliably thereafter. Monte Carlo error estimates indicate that stress estimates can be made for wind speeds greater than 25 m s^{-1}; the error decreases with greater wind speeds. Downwind and crosswind drag coefficients are computed from the computed stress and the mapped wind data. Downwind drag coefficients increase to $3.5 \pm 0.7 \times 10^{-3}$ at 31 m s^{-1}, a value greater than most previous estimates, but decrease to $2.0 \pm 0.4 \times 10^{-3}$ for wind speeds > 45 m s^{-1}, in agreement with previous estimates. The crosswind drag coefficient of $1.6 \pm 0.5 \times 10^{-3}$ at wind speeds 30–45 m s^{-1} implies that the wind stress is about 20° clockwise from the 10-m wind vector and thus not directly downwind, as is often assumed.

1. Introduction

a. Surface wind stress and drag coefficient

Tropical cyclones with strong winds, heavy rain, and storm surges produce severe damage to coastal and inland regions annually. To improve the prediction of tropical cyclones' intensity, and the associated storm surges and precipitation, extensive studies have been devoted to typhoon–ocean interactions. The surface wind stress $\boldsymbol{\tau}$ generated by tropical cyclone winds extracts energy and momentum from the storm, limiting its intensity, but also forces ocean currents (Emanuel 1995). It is often parameterized by a drag coefficient C_d, expressed as $|\boldsymbol{\tau}| = \rho_{\mathrm{air}} C_d |\mathbf{U}_{10}|^2$, where ρ_{air} is the air density, and $|\mathbf{U}_{10}|$ is the wind velocity at 10 m above the sea surface. Previous studies suggest various empirical forms of C_d as a function of $|\mathbf{U}_{10}|$, atmospheric stability, surface roughness, surface wave height, and wave age (e.g., Charnock 1955; Dyer 1974; Johnson et al. 1998; Drennan et al. 2003). Better understanding of the surface wind stress and its parameterization C_d is thus crucial for forecasting tropical cyclones and improving the prediction of the oceanic response to them.

b. Methods to estimate surface wind stress in tropical cyclones

Most previous studies have computed C_d under tropical cyclones from atmospheric measurements. The wind speed taken by the anemometers on buoys can be used to compute the momentum flux from tropical cyclones to the ocean (e.g., Potter et al. 2015). Powell et al. (2003) and Holthuijsen et al. (2012) estimated the surface roughness length and C_d using the profiles of tropical cyclones' wind speed taken by GPS dropsondes, assuming the wind speed increases logarithmically with the height above the sea surface. Bell et al. (2012) studied the C_d using the atmospheric angular momentum budget and measurements of tropical cyclones' wind speed taken by a stepped frequency microwave radiometer (SFMR) mounted on the aircraft.

Alternatively, C_d can be estimated from the momentum flux to ocean currents by measuring velocity under tropical cyclones. Jarosz et al. (2007) and Sanford et al. (2011)

Denotes content that is immediately available upon publication as open access.

Corresponding author e-mail: Je-Yuan Hsu, jyhsu@apl.washington.edu

DOI: 10.1175/JPO-D-16-0069.1

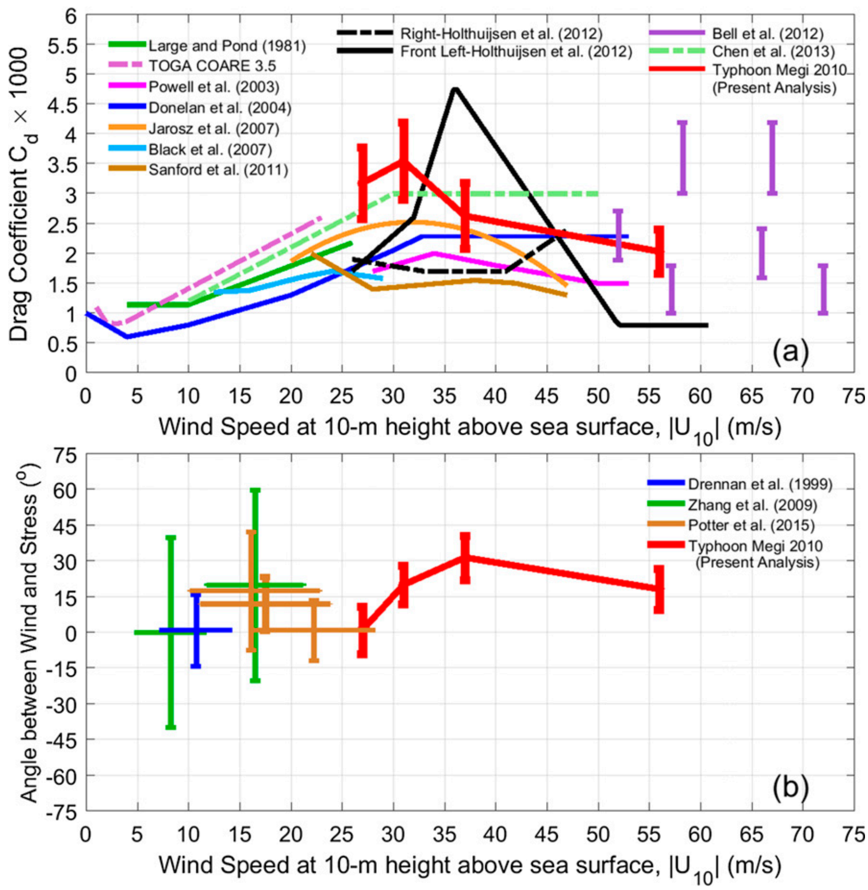

FIG. 1. (a) The drag coefficient C_d as a function of wind speed at 10 m above the sea surface $|\mathbf{U}_{10}|$ from our analysis (thick red lines) and as proposed by previous investigators (other colors). (b) Angle between the surface wind and stress vectors from our analysis (thick red) and from Drennan et al. (1999, their Fig. 6), Zhang et al. (2009, their Figs. 1 and 3), and Potter et al. (2015, their Figs. 1 and 4). Measured wind speed from these investigators is extrapolated to 10 m above the sea surface assuming a logarithmic wind profile. The horizontal and vertical bars describe the ranges of their data. The positive angle implies a stress vector that points clockwise from the wind vector.

analyzed velocity measurements taken by the ADCP on moorings and three electromagnetic autonomous profiling explorer (EM-APEX) floats under tropical cyclones, respectively. Using the depth-integrated linear momentum equation (hereinafter, the linear momentum budget method), they estimated the magnitude of surface wind stress and parameterized C_d as a function of wind speed. The present study uses a similar approach to compute C_d under Typhoon Megi. Note that the C_d estimated using the oceanic velocity measurements as a bottom-up approach may be inconsistent with that using the atmospheric wind speed measurements.

c. Previous drag coefficient estimation methods

The Tropical Ocean Global Atmosphere Coupled Ocean–Atmosphere Response Experiment (TOGA COARE) has made observations of the air–sea flux from low to moderate wind speeds ($|\mathbf{U}_{10}| < 20\,\mathrm{m\,s^{-1}}$) using ships and buoys since the 1990s (Edson et al. 2013). Employing the TOGA COARE bulk algorithm 3.5 (Edson et al. 2013), the drag coefficient depends more strongly on wind speed than atmospheric stability. It increases from 1×10^{-3} to 2.4×10^{-3}, >100%, as the wind speed $|\mathbf{U}_{10}|$ increases from 5 to $20\,\mathrm{m\,s^{-1}}$, whereas the drag coefficient changes only about 5% when the atmospheric stability (z/L, where z is the height above the sea surface and L is the Monin–Obukhov length) varies from −1 to −0.2. Large and Pond (1981) report that C_d is a constant for $|\mathbf{U}_{10}| = 4$–$11\,\mathrm{m\,s^{-1}}$ and increases linearly with wind speed for $|\mathbf{U}_{10}| = 11$–$25\,\mathrm{m\,s^{-1}}$ (Fig. 1a). The latest TOGA COARE bulk algorithm 3.5 also proposes that C_d increases linearly with wind speed for $|\mathbf{U}_{10}| = 6$–$25\,\mathrm{m\,s^{-1}}$ (Edson et al. 2013), with a value slightly greater than that reported by Large and Pond (1981).

The parameterization of C_d in tropical cyclone wind conditions has been studied extensively using atmospheric and oceanic measurements, laboratory experiments, and model simulations (e.g., Powell et al. 2003; Donelan et al. 2004; Jarosz et al. 2007; Black et al. 2007; Sanford et al. 2011; Holthuijsen et al. 2012; Chen et al. 2013). These studies generally support the linear increase of C_d with wind speed for $|\mathbf{U}_{10}| < 25\,\mathrm{m\,s^{-1}}$. For stronger winds, $|\mathbf{U}_{10}| > 30\,\mathrm{m\,s^{-1}}$, C_d is "saturated," either remaining at a constant value or decreasing with wind speed (Fig. 1a). Bell et al. (2012) quantified C_d at wind speeds greater than $52\,\mathrm{m\,s^{-1}}$ in two hurricanes and report that C_d scattered for extremely high wind speeds $|\mathbf{U}_{10}| = 52$–$72\,\mathrm{m\,s^{-1}}$, with a mean of 2.4×10^{-3} and a standard deviation of 1.1×10^{-3}.

Recent studies suggest that the parameterization of C_d by $|\mathbf{U}_{10}|$ varies in different sectors of the tropical cyclone. Holthuijsen et al. (2012) report that a maximum C_d ($\sim 4.6 \times 10^{-3}$) is located at the front-left quadrant of the tropical cyclone, and a minimum ($\sim 1.7 \times 10^{-3}$) is located on the right side for $|\mathbf{U}_{10}| = 30$–$40\,\mathrm{m\,s^{-1}}$. Chen et al. (2013) used an atmosphere–wave–ocean coupled model to investigate C_d under Hurricane Frances. In contrast to results reported by Holthuijsen et al. (2012), they conclude that C_d is generally greater at the front-right quadrant of tropical cyclones than at the left side. They suggest that the variation in different quadrants is due to the spatial variability of surface waves forced by the rapid change of tropical cyclones' wind.

Most previous studies assume that the crosswind stress is insignificant compared to the downwind stress (e.g., Large and Pond 1981). Recent field experiments investigating the effect of surface waves on surface wind stress report significant crosswind stress (Geernaert 1988; Drennan et al. 1999; Grachev et al. 2003; Zhang et al. 2009; Potter et al. 2015). Zhang et al. (2009) report that the direction difference between the surface wind and stress vectors varies from $-40°$ to $60°$ for wind speeds 5–$20\,\mathrm{m\,s^{-1}}$ (Fig. 1b). Under tropical cyclones, extremely complex surface waves can be generated. The effect of surface waves on the crosswind stress has been studied using numerical models coupled with the surface wave field in tropical cyclones (Moon et al. 2004; Chen et al. 2013; Reichl et al. 2014). Chen et al. (2013) report that the direction difference between the surface wind and the stress vectors is more than 20° within the eyewall of a tropical cyclone, again suggesting a significant crosswind stress.

Studies report a large variability in C_d at wind speeds greater than $25\,\mathrm{m\,s^{-1}}$ (Fig. 1a) and contradictory results for C_d distribution in different sectors of tropical cyclones (Holthuijsen et al. 2012; Chen et al. 2013). Numerical model studies show significant crosswind stress under tropical cyclones, but field observations are meager and vary greatly.

d. *Drag coefficient study of Typhoon Megi 2010*

In 2010 an international joint experiment, the Impact of Typhoons on the Ocean in the Pacific (ITOP), was conducted in the western Pacific to study the oceanic response to and recovery from tropical cyclones (D'Asaro et al. 2014). One of the primary scientific goals was to investigate surface wind stress under extreme wind conditions. During ITOP, seven EM-APEX floats were deployed to the right of Typhoon Megi's track, a category 5 typhoon in October 2010. Following Sanford et al. (2011), we estimate downwind and crosswind stress using velocity measurements taken by these floats via the linear momentum budget method.

Typhoon Megi and EM-APEX float measurements are described in section 2, and the linear momentum budget method is discussed in section 3. The downwind and crosswind drag coefficients are defined. The tidal and low-frequency current velocities may introduce uncertainties to wind stress estimates and are discussed in section 4. The apparent drag coefficients are estimated in section 5. The Price–Pinkel–Weller model (PWP3D) has been used to study the ocean momentum response to tropical cyclones (Price et al. 1994; Sanford et al. 2011). Here, the PWP3D is used to assess the assumed linear momentum budget to estimate surface wind stress (section 6). A correction to the derived wind stress estimates is made to yield the adjusted wind stress (section 7), which is investigated using the PWP3D model. Our drag coefficient estimates and the direction difference between the surface wind and stress vectors are discussed and compared with previous studies (section 8).

2. Experiment and measurements

ITOP targeted Typhoons Fanapi and Megi using measurements taken from various atmospheric and oceanic platforms (D'Asaro et al. 2014). In this analysis, we focus on the drag coefficient estimated using measurements taken during Super Typhoon Megi only (Fig. 2a). Megi formed in the western Pacific on 12 October 2010 and intensified rapidly becoming a category 5 typhoon on 17 October (Wang and Wang 2014). Typhoon Megi moved primarily westward in the western Pacific, passed the northern Philippines on 18 October, turned northwestward into the South China Sea, and dissipated on 23 October after making landfall in China

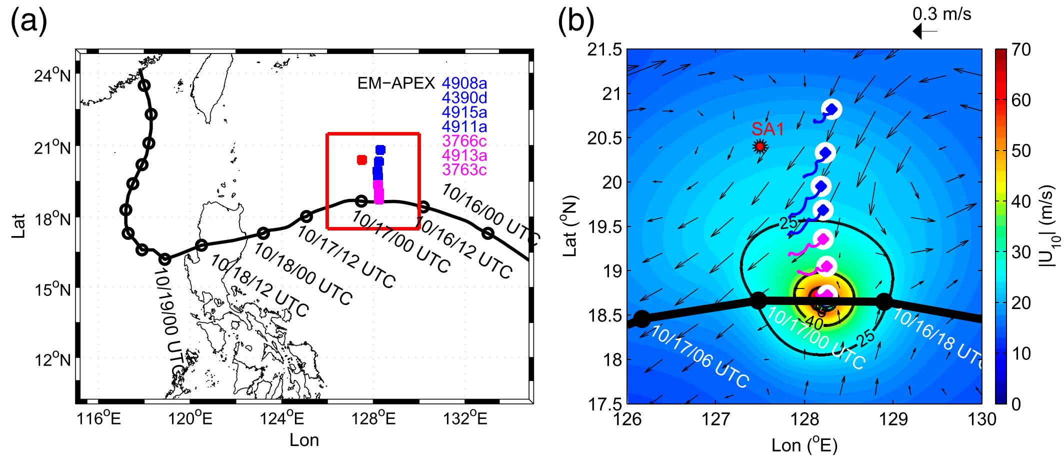

FIG. 2. (a) Typhoon Megi's track (black curve with dots), deployment positions of EM-APEX floats (blue and magenta dots), and position of mooring SA1 (red dot) and (b) the wind map of wind speed at 10 m above the sea surface (color shading) at 2030 UTC 16 Oct at the arrival time of Typhoon Megi at the float array, AVISO surface geostrophic current velocity (black arrows) on 17 Oct, EM-APEX float positions and trajectories (blue and magenta dots and curves), and mooring SA1 position (red dot). Typhoon track is labeled with time as month/day/hour UTC. Float deployment details are listed in Table 1.

(D'Asaro et al. 2014; Wang and Wang 2014). This study focuses on measurements of Megi in the western Pacific only.

Between 12 and 18 October, 221 GPS dropsondes were deployed from the C130 aircraft to measure vertical profiles of wind speed and direction (Hock and Franklin 1999), and SFMR mounted on the bottom of the C130s measured the microwave brightness temperature. The measurements of microwave brightness temperature were processed to estimate the wind speed at 10 m above the sea surface ($|\mathbf{U}_{10}|$) as described in Uhlhorn and Black (2003). These were cross calibrated and combined to construct a map of the surface winds (Fig. 2b), as described in appendix A. During the measurement period, the radius of maximum wind speed was 15 km, smaller than the average size of tropical cyclones in the western Pacific (~40 km), and the westward translation speed was ~7 m s^{-1}, faster than typical tropical cyclones at the same latitude (4–5 m s^{-1}).

Seven EM-APEX floats were deployed by a C130 aircraft, at a horizontal separation of ~25 km, along 128.3°E between 18.7° and 21°N on 16 October 2010, 1 day before the arrival of the eye of Typhoon Megi (Fig. 2a; Table 1). Floats were recovered by the R/V *Roger Revelle* on 19 October, 3 days after the deployment. Three EM-APEX floats measured the oceanic response to winds greater than 25 m s^{-1}. One float (em3763c) passed directly under the eye of Megi; the other two floats (em4913a and em3766c) passed at ~42 km and ~73 km north of Megi's eye on the right side of the storm track. Data obtained from these three floats are used to compute the surface wind stress in this study.

EM-APEX floats measure the electric and magnetic fields in the ocean (Sanford et al. 2005). The oceanic current velocity, relative to a conductivity-weighted average current $\overline{\mathbf{V}^{*}}$, is estimated using the measured electric and magnetic fields based on the principle of motional induction (Sanford et al. 1978). Absolute current velocity can be obtained by estimating $\overline{\mathbf{V}^{*}}$ using the float's GPS positions (Lien et al. 2013). The uncertainty of EM velocity measurements taken during the ITOP experiment is 0.8–1.5 cm s^{-1}, estimated using the white spectral level of the observed velocity spectra. Temperature and salinity measurements were taken by a SeaBird Electronics SBE-41 CTD sensor mounted on the top end of the floats. The vertical resolution of velocity, temperature, and salinity was 3–4 m. GPS positions and data were transmitted by Iridium satellites when floats surfaced.

Before the arrival of Megi, floats profiled vertically from near the surface to 230-m depth at a profiling speed of 0.1–0.12 m s^{-1}. Between 1000 UTC 16 October and 2100 UTC 18 October when Megi passed the float array,

TABLE 1. EM-APEX float deployment locations at the time they began profiling during the ITOP experiment.

Float name	First profiling time (UTC)	Lon (°E)	Lat (°N)
em3763c	0059 UTC 16 Oct 2010	128.3	18.7
em4913a	0052 UTC 16 Oct 2010	128.3	19.1
em3766c	0035 UTC 16 Oct 2010	128.3	19.4
em4911a	0035 UTC 16 Oct 2010	128.3	19.7
em4915a	0032 UTC 16 Oct 2010	128.3	20.0
em4390d	0025 UTC 16 Oct 2010	128.3	20.4
em4908a	0011 UTC 16 Oct 2010	128.3	20.7

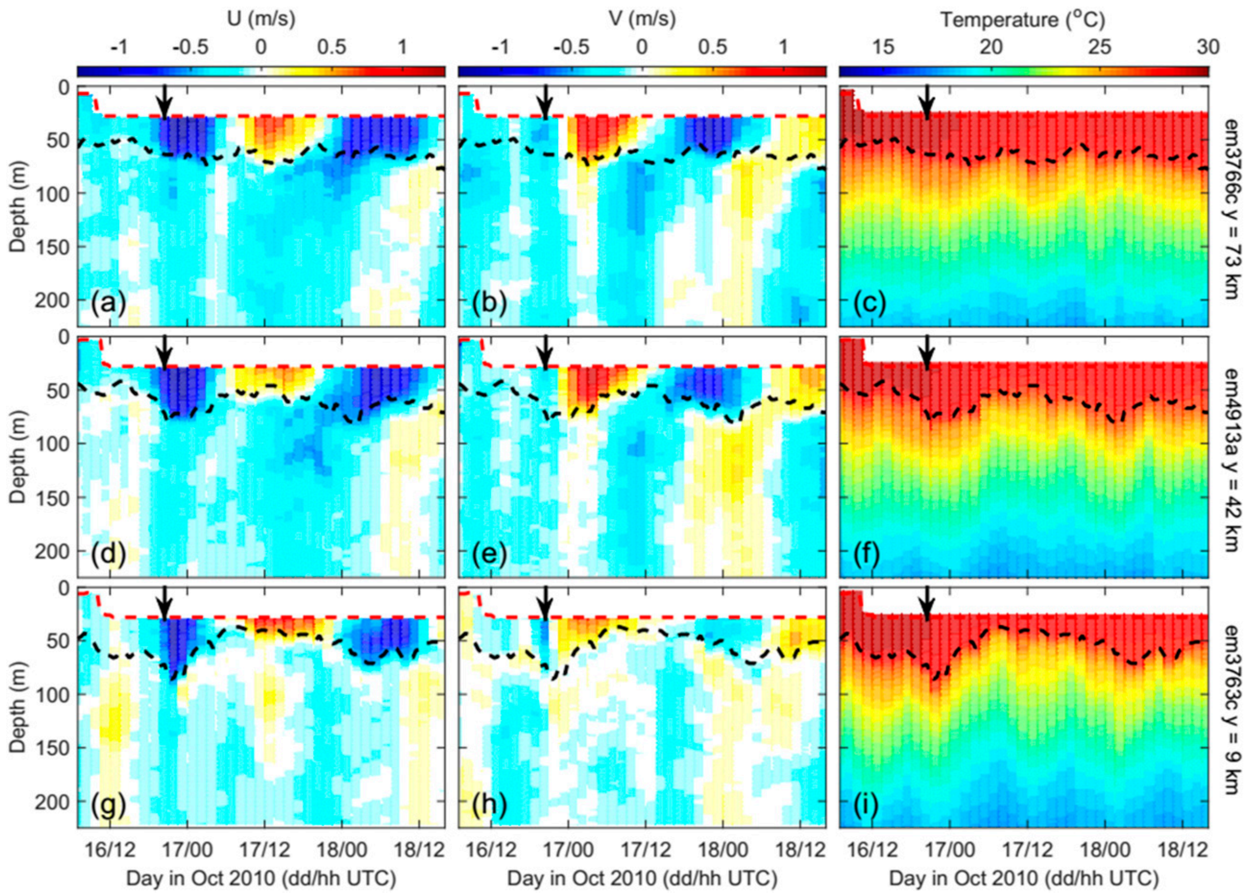

FIG. 3. (a),(d),(g) Zonal velocity, (b),(e),(h) meridional velocity, and (c),(f),(i) temperature measured by three EM-APEX floats. The dashed red lines mark the shallowest depth of float measurements. The distance of each float from Megi's track is labeled to the right of the right column. The black arrows mark the closest approach of Typhoon Megi to the float array, 2030 UTC 16 Oct. The black dashed curves represent the depth of the surface mixed layer.

EM-APEX floats profiled between 30- and 230-m depth to prevent damage by storm-induced surface waves. In the following analysis, the current velocity in the upper 30 m is assumed constant and extrapolated to the surface using the shallowest velocity measurement below 30-m depth. The floats' positions during this period are estimated using the time integration of current velocity measured by the floats.

Strong near-inertial waves were generated on the right side of Megi due to the inertial resonance of the wind pattern. At 42 km to the right of the storm track (em4913a; Fig. 2a), the near-inertial current was greater than 1 m s^{-1} (Figs. 3d,e). The surface mixed layer, defined as the shallowest depth where the density gradient is greater than 0.03 kg m^{-4} and the density is greater than the surface values by more than 0.3 kg m^{-3}, deepened by more than 20 m, from ~40- to 70-m depth, within one-half day after Megi's eye arrived at the float array, ~2030 UTC 16 October. The base of the surface mixed layer oscillated by ~10 m near the inertial period due to the convergence and divergence of near-inertial waves, in agreement with observations reported by Gill (1984). The surface mixed layer cooled from 29.3° to 28.2°C in 1 day, presumably due to vertical mixing (Sanford et al. 2011).

The background oceanic current measured by the floats from the north to Megi's track varied from 0.4 (em3766c) to 0.1 m s^{-1} (em3763c) at 12 h before Megi's arrival (Fig. 3), consistent with the surface geostrophic current estimated from AVISO (Fig. 2b). Tidal currents were also present, though at velocities less than inertial waves, especially in the surface mixed layer. Detailed analysis of the tides is given in appendix B.

Several moorings were deployed during ITOP on the prevailing path of tropical cyclones (D'Asaro et al. 2014). One of the moorings, SA1, was located about 200 km north of Typhoon Megi's track. The mooring was equipped with a 75-kHz upward-looking ADCP to measure current velocity between 50- and 550-m depth. In the following analysis, mooring velocity measurements will be used to quantify the tidal current during the observational period.

3. Estimates of surface wind stress and drag coefficients

a. Linear momentum budget method

Following Sanford et al. (2011), we estimate surface wind stress using the depth-integrated linear momentum balance and the observed current velocity profiles taken by the EM-APEX floats. The momentum equation for a Boussinesq fluid is

$$\frac{\partial \mathbf{u}}{\partial t} + \mathbf{u}\cdot\nabla\mathbf{u} + f\hat{\mathbf{k}}\times\mathbf{u} = -\frac{1}{\rho_0}\nabla p + \frac{1}{\rho_0}\frac{\partial \boldsymbol{\tau}}{\partial z} - \frac{\rho}{\rho_0}g\hat{\mathbf{k}}, \tag{1}$$

where $\mathbf{u} = u\hat{\mathbf{i}} + v\hat{\mathbf{j}} + w\hat{\mathbf{k}}$ is the ocean current velocity vector. The $\nabla = \partial/\partial x\hat{\mathbf{i}} + \partial/\partial y\hat{\mathbf{j}} + \partial/\partial z\hat{\mathbf{k}}$ is the gradient operator, where $\hat{\mathbf{i}}$, $\hat{\mathbf{j}}$, and $\hat{\mathbf{k}}$ are the unit vectors in east, north, and upward vertical directions, respectively, g is the gravity, f is the local Coriolis frequency of $\sim 5\times 10^{-5}\,\mathrm{rad\,s^{-1}}$ at 20°N, p is the pressure, ρ_0 is the Boussinesq density, ρ is the in situ density, and $\boldsymbol{\tau}$ is the stress vector.

Defining the horizontal current velocity and gradient operator as $\mathbf{v}_h = u\hat{\mathbf{i}} + v\hat{\mathbf{j}}$ and $\nabla_h = \partial/\partial x\hat{\mathbf{i}} + \partial/\partial y\hat{\mathbf{j}}$, respectively, the depth-integrated momentum equation from the sea surface to a depth $-H$ becomes

$$\int_{-H}^{0}\left(\frac{\partial \mathbf{v}_h}{\partial t} + \mathbf{v}_h\nabla_h\cdot\mathbf{v}_h + \mathbf{v}_h\cdot\nabla_h\mathbf{v}_h + f\hat{\mathbf{k}}\times\mathbf{v}_h + \frac{1}{\rho_0}\nabla_h p\right)dz = \frac{(\boldsymbol{\tau}_o - \boldsymbol{\tau}_{-H})}{\rho_0} + w_{-H}\mathbf{v}_{-H}, \tag{2}$$

where $\boldsymbol{\tau}_o$ is the surface wind stress, and $\boldsymbol{\tau}_{-H}$ and $\mathbf{v}_{-H}$ are the turbulent stress and horizontal velocity at $z = -H$, respectively. We assume that the vertical velocity vanishes at the sea surface. Following Sanford et al. (2011), we choose $H = 150$ m and assume that $\boldsymbol{\tau}_{-H}$ and $w_{-H}\mathbf{v}_{-H}$ are zero. These assumptions are justified by results from PWP3D model simulations (section 4). The depth-integrated momentum equation is therefore simplified as

$$\int_{-H}^{0}\left(\frac{\partial \mathbf{v}}{\partial t} + f\hat{\mathbf{k}}\times\mathbf{v} + \mathbf{v}\nabla_h\cdot\mathbf{v} + \mathbf{v}\cdot\nabla_h\mathbf{v} + \frac{1}{\rho_0}\nabla_h p\right)dz = \frac{\boldsymbol{\tau}}{\rho_0}. \tag{3}$$

Here, we have dropped the subscripts for the horizontal current velocity $\mathbf{v}$ and surface wind stress $\boldsymbol{\tau}$ for convenience.

Sanford et al. (2011) estimate the surface wind stress $\tilde{\tau}$, assuming the balance between the first two terms in Eq. (3) with the wind stress, that is,

$$\tilde{\tau} = \boldsymbol{\tau} + \Delta\boldsymbol{\tau} = \rho_0\int_{-H}^{0}\left(\frac{\partial \mathbf{v}}{\partial t} + f\hat{\mathbf{k}}\times\mathbf{v}\right)dz, \tag{4}$$

where $\Delta\boldsymbol{\tau}$ is the uncertainty of $\tilde{\tau}$. The $\Delta\boldsymbol{\tau}$ represents the error in estimates of surface wind stress because of either the neglect of nonlinear terms and pressure gradient, that is, the third–fifth terms on the left side of Eq. (3), or the existence of non-wind-driven ocean current measured by the floats. The latter is discussed in section 4. To distinguish the estimates of surface wind stress using the linear momentum budget from the true wind stress $\boldsymbol{\tau}$, the $\tilde{\tau}$ in Eq. (4) is termed apparent surface wind stress. Sanford et al. (2011) assume a linear momentum balance with negligible pressure gradient and nonlinear terms, that is, $\Delta\boldsymbol{\tau} = 0$, so $\tilde{\tau} = \boldsymbol{\tau}$. PWP3D numerical modeling is used to investigate the validity of this assumption (section 6). The differencing terms in the momentum budget [Eqs. (3) and (4)] are computed in the second-order scheme in this study.

b. Downwind and crosswind drag coefficients

Recent studies (e.g., Reichl et al. 2014; Chen et al. 2013) report that the surface wind stress may have a significant crosswind component. In this analysis, the vector $\boldsymbol{\tau}$ on the ocean surface can be projected to the respective directions along and perpendicular to the wind vector at 10-m height above the sea surface $\mathbf{U}_{10}$ as

$$\boldsymbol{\tau} = \tau_{\parallel}\widehat{\mathbf{U}_{10\parallel}} + \tau_{\perp}\widehat{\mathbf{U}_{10\perp}}, \tag{5}$$

where $\widehat{\mathbf{U}_{10\parallel}}$ and $\widehat{\mathbf{U}_{10\perp}}$ are unit vectors along and perpendicular to the $\mathbf{U}_{10}$, and $\tau_{\parallel}$ and $\tau_{\perp}$ are the projected stress at the downwind and crosswind directions, respectively. The angle ϕ between $\mathbf{U}_{10}$ and the surface wind stress $\boldsymbol{\tau}$ is defined as

$$\phi = \tan^{-1}\frac{\tau_{\perp}}{\tau_{\parallel}}. \tag{6}$$

The quantities $\tau_{\perp}$ and ϕ are greater than zero when the orientation of $\boldsymbol{\tau}$ is clockwise from the $|\mathbf{U}_{10}|$. Following previous studies (Smith 1980; Powell et al. 2003; Donelan et al. 2004), we parameterize $\tau_{\parallel}$ and $\tau_{\perp}$ by wind speed and define the downwind and crosswind drag coefficients as

$$C_{\parallel} = \frac{\tau_{\parallel}}{\rho_{\mathrm{air}}|\mathbf{U}_{10}|^2};\quad C_{\perp} = \frac{\tau_{\perp}}{\rho_{\mathrm{air}}|\mathbf{U}_{10}|^2};\quad C_d = \sqrt{C_{\parallel}^2 + C_{\perp}^2}. \tag{7}$$

Here, C_d is the magnitude of the drag coefficient. The estimates of downwind and crosswind drag coefficients computed using the linear momentum budget expressed in Eq. (4) are termed apparent downwind and crosswind drag coefficients $\widetilde{C_\parallel}$ and $\widetilde{C_\perp}$.

4. Storm-induced current velocity under Typhoon Megi

EM-APEX float velocity measurements $\mathbf{v}$ taken before the arrival of Typhoon Megi's eye are used to estimate the surface wind stress and drag coefficient using the depth-integrated linear momentum budget [Eq. (4)]. The primary constituents of current velocity can be assumed as

$$\mathbf{v} = \mathbf{v}_{\text{wind}} + \mathbf{v}_{\text{tide}} + \mathbf{v}_{\text{low}} + \boldsymbol{\epsilon},$$

where $\mathbf{v}_{\text{wind}}$ is the velocity of wind-driven current, $\mathbf{v}_{\text{tide}}$ is the velocity of tides, $\mathbf{v}_{\text{low}}$ is the velocity of low-frequency currents, constant in amplitude and direction for at least a half day, such as the surface geostrophic current, and $\boldsymbol{\epsilon}$ is the instrumental noise in the velocity measurements.

Only the wind-driven ocean current velocity $\mathbf{v}_{\text{wind}}$ should be used to estimate surface wind stress in Eq. (4). The background currents, such as tides $\mathbf{v}_{\text{tide}}$ and low-frequency currents $\mathbf{v}_{\text{low}}$, which are not directly forced by Megi, will cause the linear momentum budget to unbalance. For example, the depth-integrated linear momentum of a diurnal barotropic tide K_1 with amplitude $0.1\,\text{m}\,\text{s}^{-1}$ from the ocean surface to 150-m depth is $\sim 0.7\,\text{N}\,\text{m}^{-2}$, leading to an error of ~20% in surface wind stress estimates if $C_d = 4\times10^{-3}$ at $|\mathbf{U}_{10}| = 30\,\text{m}\,\text{s}^{-1}$. The magnitude of low-frequency currents can also influence the Coriolis rotation term in the linear momentum budget. The integrated momentum of randomly distributed $\boldsymbol{\epsilon}$ in the linear momentum budget was investigated but is negligible compared to the contributions of $\mathbf{v}_{\text{wind}}$, $\mathbf{v}_{\text{tide}}$, and $\mathbf{v}_{\text{low}}$.

To estimate the apparent surface wind stress $\tilde{\tau}$ using the wind-driven current velocity $\mathbf{v}_{\text{wind}}$, the tides $\mathbf{v}_{\text{tide}}$ and low-frequency currents $\mathbf{v}_{\text{low}}$ are both estimated and removed from EM-APEX velocity measurements. The amplitude and phase of tides at the float locations are estimated by harmonic fitting of the velocity measurements between 200- and 220-m depth (appendix B, section a) and then used to extrapolate tides to the ocean surface by assuming the first-mode baroclinic tide. The uncertainty of estimating $\mathbf{v}_{\text{tide}}$ is primarily due to vertical phase propagation and amplitude difference in tidal extrapolation, implemented by the analysis of tides on the mooring SA1 (appendix B, section b). The low-frequency current is estimated by averaging the profiles of $(\mathbf{v} - \mathbf{v}_{\text{tide}})$ at different selected periods, assuming the $\mathbf{v}_{\text{wind}}$ had not been forced by Megi (appendix B, section c). The uncertainty of estimating $\mathbf{v}_{\text{low}}$ is affected by the estimates of $\mathbf{v}_{\text{tide}}$ and the selected averaging period.

Simulations of 40 000 normally distributed $(\mathbf{v}_{\text{tide}} + \mathbf{v}_{\text{low}})$ are generated in the stochastic simulation (appendix B, section d) and removed from each of the observed EM-APEX float velocity profiles so as to generate 40 000 realizations of apparent wind-forced velocity profiles $\widetilde{\mathbf{v}_{\text{wind}}}$.

5. Estimates of apparent drag coefficients

The $|\mathbf{U}_{10}|$ for the computation of drag coefficients is simulated in the normal distribution using the measured wind speed and root-mean-square (RMS) error; RMS is $\sim 4\,\text{m}\,\text{s}^{-1}$ outside Megi's eyewall, and $\sim 5\,\text{m}\,\text{s}^{-1}$ within the eyewall (appendix A, section a). Using the $\widetilde{\mathbf{v}_{\text{wind}}}$ in the linear momentum budget [Eq. (4)], 40 000 estimates of surface wind stress are computed and parameterized as apparent drag coefficients. The mean and standard deviation of apparent drag coefficients $\widetilde{C_\parallel}$ and $\widetilde{C_\perp}$ are computed for each EM-APEX float velocity profile (Figs. 4a,b).

Estimates of apparent drag coefficient are presented as the function of wind speed at 10 m above the sea surface $|\mathbf{U}_{10}|$ (small dots and thin vertical lines in Fig. 4). The standard deviations of estimates of apparent drag coefficients $\widetilde{C_\parallel}$ and $\widetilde{C_\perp}$ (vertical lines) are generally greater than 1.5×10^{-3} for $|\mathbf{U}_{10}| = 25$–$30\,\text{m}\,\text{s}^{-1}$. The large uncertainty in estimates of drag coefficient for $|\mathbf{U}_{10}| < 25\,\text{m}\,\text{s}^{-1}$ is due primarily to contamination by the tides and mean currents on estimates of wind-driven currents. We discuss drag coefficients for $|\mathbf{U}_{10}| > 25\,\text{m}\,\text{s}^{-1}$ exclusively in the following.

To summarize the effect of wind speed on apparent drag coefficients, we further average drag coefficients in different bins of wind speed ($\pm 2\,\text{m}\,\text{s}^{-1}$ at $|\mathbf{U}_{10}| = 27\,\text{m}\,\text{s}^{-1}$, $\pm 3\,\text{m}\,\text{s}^{-1}$ at $|\mathbf{U}_{10}| = 31\,\text{m}\,\text{s}^{-1}$, $\pm 3\,\text{m}\,\text{s}^{-1}$ at $|\mathbf{U}_{10}| = 37\,\text{m}\,\text{s}^{-1}$, and $\pm 9\,\text{m}\,\text{s}^{-1}$ at $|\mathbf{U}_{10}| = 56\,\text{m}\,\text{s}^{-1}$). We use the mean and standard deviation of apparent drag coefficients from each profile of EM-APEX floats to generate 1000 simulations assuming a normal distribution. Within each bin of wind speed, the apparent drag coefficient averages are computed using the generated simulations from at least three different profiles, and then the mean and the standard deviation of the apparent drag coefficient averages are computed. The estimates of $\widetilde{C_\parallel}$ are more than 3×10^{-3} for $|\mathbf{U}_{10}| = 30$–$40\,\text{m}\,\text{s}^{-1}$. The $\widetilde{C_\perp}$ and the angle between wind and stress ϕ are significantly different from zero, indicating the crosswind component of surface wind stress is not negligible.

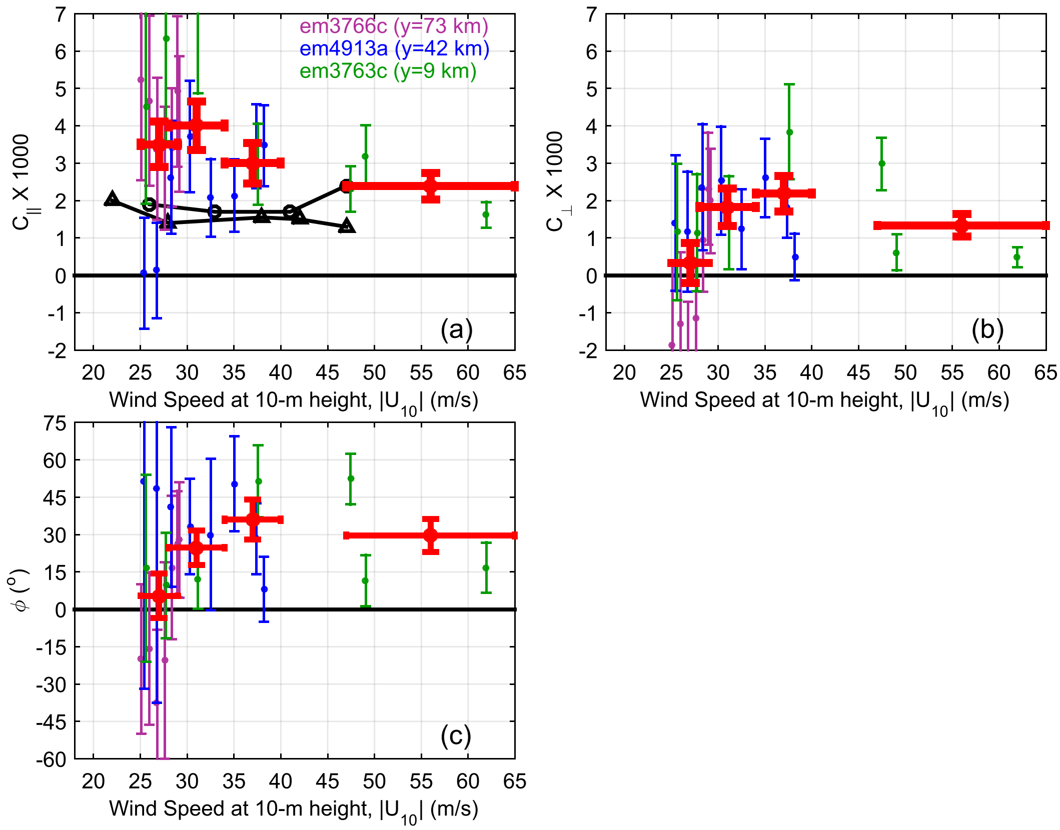

FIG. 4. (a) Apparent downwind drag coefficient $C_{\|}$, (b) crosswind drag coefficient $C_{\perp}$, and (c) angle between surface wind stress vector and wind for $|\mathbf{U}_{10}| > 22\,\mathrm{m\,s^{-1}}$. This intermediate product is further corrected to give the final results shown in Fig. 1. The dots and vertical bars represent the mean of apparent drag coefficients and the plus or minus one standard deviation, computed using profiles of velocity measurements taken from three EM-APEX floats (purple, blue, and green colors) at different distances from the storm track (labeled). The drag coefficients reported by Sanford et al. (2011) and Holthuijsen et al. (2012) are shown in (a) as black lines with circles and triangles, respectively. Red dots show the averages of apparent drag coefficients in bins of different wind speeds (horizontal lines). The vertical red line represents the plus or minus one standard deviation of apparent drag coefficient averages.

6. PWP3D model

The apparent drag coefficient under Typhoon Megi is estimated assuming balance of the linear momentum budget. Simulations of oceanic response under Typhoon Megi in the PWP3D model are used to validate the assumption of linear momentum balance here and to correct the apparent drag coefficient due to the neglect of nonlinear and pressure gradient terms (section 7).

a. Model description

Price et al. (1994) developed the PWP3D numerical model using momentum, continuity, temperature, and salinity equations to study oceanic responses to moving tropical cyclones. The initial temperature and salinity fields are assumed horizontally homogeneous. In the following model simulations, horizontally and temporally averaged vertical profiles of EM-APEX float measurements of temperature and salinity taken within 18–19 h before the arrival of Megi's eye are used as the initial conditions. The horizontal spatial resolution is 3 km, and the temporal resolution is 180 s. The spatial domain of the ocean is ±375 km in the zonal direction and ±300 km in the meridional direction. The vertical resolution is 5 m from the ocean surface to 300-m depth.

In the model, vertical turbulent mixing is parameterized using the bulk Richardson number $\mathrm{Ri}_b = -(g\Delta\rho h)/[\rho_0(\Delta v)^2]$ and the gradient Richardson number $\mathrm{Ri}_g = [-g(\partial\rho/\partial z)]/[\rho_0(\partial v/\partial z)^2]$, where Δv and $\Delta\rho$ are the difference of velocity and density, respectively, across the base of the surface mixed layer h (Price et al. 1986). In the PWP3D model, the turbulent mixing is enforced when $\mathrm{Ri}_g < 0.25$, or $\mathrm{Ri}_b < 0.65$, and the momentum and mass are mixed until Ri_g and Ri_b are beyond their stability criteria. For the model simulation, the spatial differencing terms are computed in the second-order scheme, and the leapfrog-trapezoidal method is used for the temporal integration (Price et al. 1994). Solar radiation is assumed as a sinusoidal function with a peak of $500\,\mathrm{W\,m^{-2}}$ at noon and zero at midnight. Longwave radiation is computed using the Boltzmann constant and sea surface temperature assuming the blackbody (Price et al. 1986). Constant values of dry (26°C) and wet (25°C) bulb air temperature in tropical cyclones are assumed (Sanford et al. 2011). The sensible and latent heat flux are computed using the wind speed and sea surface temperature in the model.

For Typhoon Megi's wind forcing in the model, the storm's wind speed and direction are interpolated linearly in time, moving in the real translation track and passing the grid point at the center of the spatial domain at 2030 UTC 18 October. The wind speed at the floats' positions in the model simulations is the same as the observations (Figs. 7g,h,i). The surface wind stress for $|\mathbf{U}_{10}| < 25\,\mathrm{m\,s^{-1}}$ in all simulations presented in this study is computed using the drag coefficient parameterization proposed by Large and Pond (1981) and mapped $|\mathbf{U}_{10}|$, assuming no crosswind stress.

b. Model simulations and momentum budget

In the first model simulation presented in this study (hereafter referred to as simulation A), the surface wind stress $\boldsymbol{\tau}$ in the model for $|\mathbf{U}_{10}| > 25\,\mathrm{m\,s^{-1}}$ is computed using the mapped $|\mathbf{U}_{10}|$ advected over the ocean and our estimates of apparent downwind drag coefficient but assuming no crosswind stress. Results of PWP3D model simulations of oceanic currents at three float positions as Megi approached the float array show the surface wind stress increasing and strong currents generated in the surface mixed layer (Fig. 5). At the arrival time of Megi, the simulated currents of $\sim 1.5\,\mathrm{m\,s^{-1}}$ are similar to those observed by floats (Fig. 3), and the modeled mixed layer deepening, $\sim 30\,\mathrm{m}$, is consistent with the observed deepening at the float on the track of Megi (em3763c).

The estimates of surface wind stress computed from Eqs. (3) and (4) are compared with the input surface wind stress (Fig. 5). The estimates of surface wind stress from Eq. (3) agree very well with the input surface wind stress, indicating that the momentum equation is implemented correctly and supporting the choice to neglect turbulent fluxes at 150-m depth in the model. Furthermore, the estimates of surface wind stress from Eq. (4) (the depth-integrated linear momentum budget) agree with the input surface wind stress with an uncertainty of <10% only before the arrival of the storm's eye. The agreement within Megi's eyewall and after the passage of Megi's eye is poor because the pressure gradient and nonlinear advection terms induced by Typhoon Megi are important, as suggested by Sanford et al. (2011). Based on PWP3D model results, drag coefficient estimates using Eq. (4) are reliable only before the arrival of Typhoon Megi, and some corrections near the eyewall of Megi are required. Note that variations in air temperature or solar radiation have little effect on the momentum budget balance. The estimate of surface wind stress using the linear momentum equation varies less than 1%, even with a change of ±3°C in air temperature or an insolation peak increase from 500 to $1000\,\mathrm{W\,m^{-2}}$.

Because the nonlinear and pressure gradient terms at two floats near Megi's track (em4913a and em3763c) led to an uncertainty of <15% before the passage of Megi's eye, another PWP3D model run at the float positions of em3763c (9 km from Megi's eye) was performed to investigate the corrections to the assumed linear momentum balance (section 7).

7. Estimates of adjusted drag coefficients

In simulation A (section 6), the downwind component of surface wind stress is computed using the mapped $|\mathbf{U}_{10}|$ and apparent downwind drag coefficient for $|\mathbf{U}_{10}| > 25\,\mathrm{m\,s^{-1}}$ but assuming no crosswind stress. The nonlinear and pressure gradient terms, which are excluded from the estimates of apparent drag coefficients in the linear momentum budget [Eq. (4)], $\mathbf{v}\nabla_h \cdot \mathbf{v}, \mathbf{v} \cdot \nabla_h \mathbf{v}$ and $(1/\rho_0)\nabla_h p$, are significant near Megi's track even before the arrival of the storm (Figs. 6a–c). Neglecting nonlinear and pressure gradient terms causes $\widetilde{C_\parallel}$ to be overestimated by $<0.4 \times 10^{-3}$ (~10% at the peak) and $\widetilde{C_\perp}$ to be overestimated by 0.5×10^{-3} at wind speeds greater than $25\,\mathrm{m\,s^{-1}}$. We subtract the effects of nonlinear and pressure gradient terms on drag coefficients (the difference between green dots and black curve in Fig. 6b and between purple dots and black line in Fig. 6c) from our estimates of apparent downwind and crosswind drag coefficients (section 5) and call these the adjusted downwind and crosswind drag coefficients.

Another simulation (simulation B) computes the surface wind stress using the mapped $|\mathbf{U}_{10}|$ and adjusted downwind and crosswind drag coefficients for $|\mathbf{U}_{10}| > 25\,\mathrm{m\,s^{-1}}$ (black curves in Figs. 6e,f). Drag coefficients computed using Eq. (4) (green dots and purple dots in Figs. 6e,f) agree well with the apparent drag coefficients discussed in section 5 (red dots with vertical bars in Figs. 6e,f), suggesting that the adjusted drag coefficients (black curves in Figs. 6e,f) are the better estimates of the true drag coefficients.

Table 2 summarizes the estimated adjusted drag coefficients in Typhoon Megi. The $C_\parallel$ is about 3.2×10^{-3}

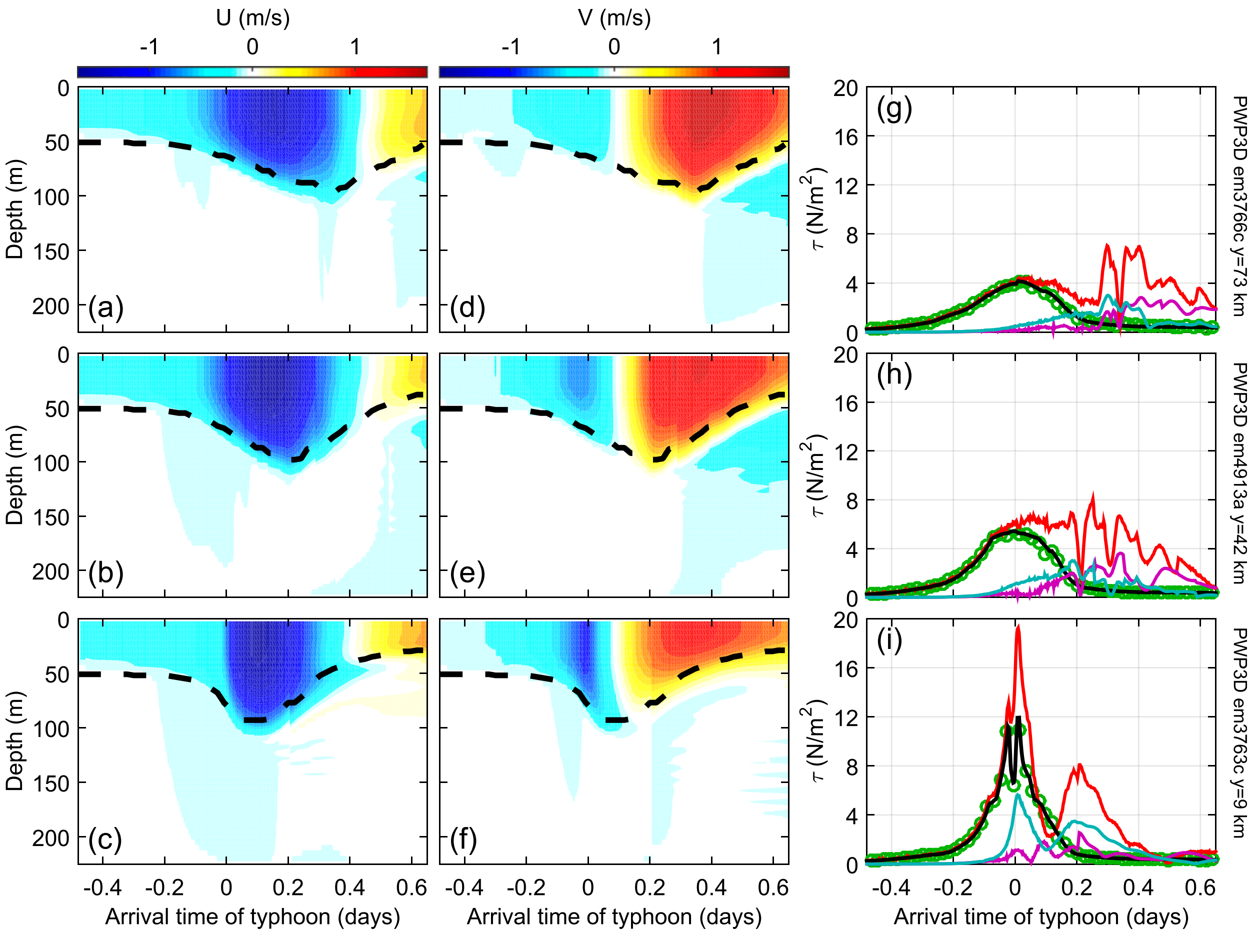

FIG. 5. (a)–(c) PWP3D model simulations of zonal current velocity, (d)–(f) meridional current velocity, (g)–(i) estimated surface wind stress via momentum budget and linear momentum budget at three float positions. Distances of floats from Megi's track are labeled to the right of the right column. Time is relative to the arrival of Typhoon Megi's eye at the float array. Black dashed curves in (a)–(f) represent the base of the surface mixed layer. Black lines in (g)–(i) show the surface wind stress computed using observed winds in Typhoon Megi and the parameterization of apparent downwind drag coefficient. Green circles in (g)–(i) are the estimates of surface wind stress computed using the depth-integrated momentum budget [Eq. (3)]. Red curves are the estimates of surface wind stress computed using the depth-integrated linear momentum budget [Eq. (4)]. Purple curves are the pressure gradient term $(1/\rho_0)\nabla_h p$ in the depth-integrated momentum budget [Eq. (3)], and cyan curves are the sum of nonlinear advection terms $\mathbf{v}\nabla_h \cdot \mathbf{v}$ and $\mathbf{v} \cdot \nabla_h \mathbf{v}$ in the depth-integrated momentum budget [Eq. (3)].

at $|\mathbf{U}_{10}| = 27\,\mathrm{m\,s^{-1}}$, reaches its peak of 3.5×10^{-3} at $|\mathbf{U}_{10}| = 31\,\mathrm{m\,s^{-1}}$, and decreases to 2.0×10^{-3} for $|\mathbf{U}_{10}| > 55\,\mathrm{m\,s^{-1}}$. The saturation of $C_\parallel$ in extreme wind conditions is significant, decreasing about 50%. The $C_\perp$ is about zero for $|\mathbf{U}_{10}| < 27\,\mathrm{m\,s^{-1}}$, reaches its peak of 1.6×10^{-3} at $|\mathbf{U}_{10}| = 37\,\mathrm{m\,s^{-1}}$, and decreases to 0.7×10^{-3} for $|\mathbf{U}_{10}| > 45\,\mathrm{m\,s^{-1}}$. The $C_\perp$ also decreases more than 50% for $|\mathbf{U}_{10}| > 37\,\mathrm{m\,s^{-1}}$, but the orientation offset between stress and $|\mathbf{U}_{10}|$ changes only slightly, from 30° to 20° for $|\mathbf{U}_{10}| = 37$–$56\,\mathrm{m\,s^{-1}}$.

To further validate our estimates of adjusted $C_\parallel$ and $C_\perp$ (Fig. 1; Table 2) at the front-right quadrant of Typhoon Megi, we compute the depth-integrated time rate change of horizontal momentum and the Coriolis force (Fig. 7), that is, $\int \partial\mathbf{v}/\partial t\,dz$ and $\int (f \times \mathbf{v})\,dz$, using float observations and then compare our results with those from simulations B and C (Fig. 7). The downwind component of surface wind stress in simulation C is computed using the mapped $|\mathbf{U}_{10}|$ and the C_d reported by Holthuijsen et al. (2012) for $|\mathbf{U}_{10}| > 25\,\mathrm{m\,s^{-1}}$ but assuming no crosswind stress. The correlation coefficient of depth-integrated linear momentum components between simulation B results and float observations for $|\mathbf{U}_{10}| > 25\,\mathrm{m\,s^{-1}}$ is 0.83. This is slightly better than that between simulation C results and observations (0.68; Fig. 8). That is, simulation results using our adjusted drag coefficients agree with observations better than those using the C_d reported by Holthuijsen

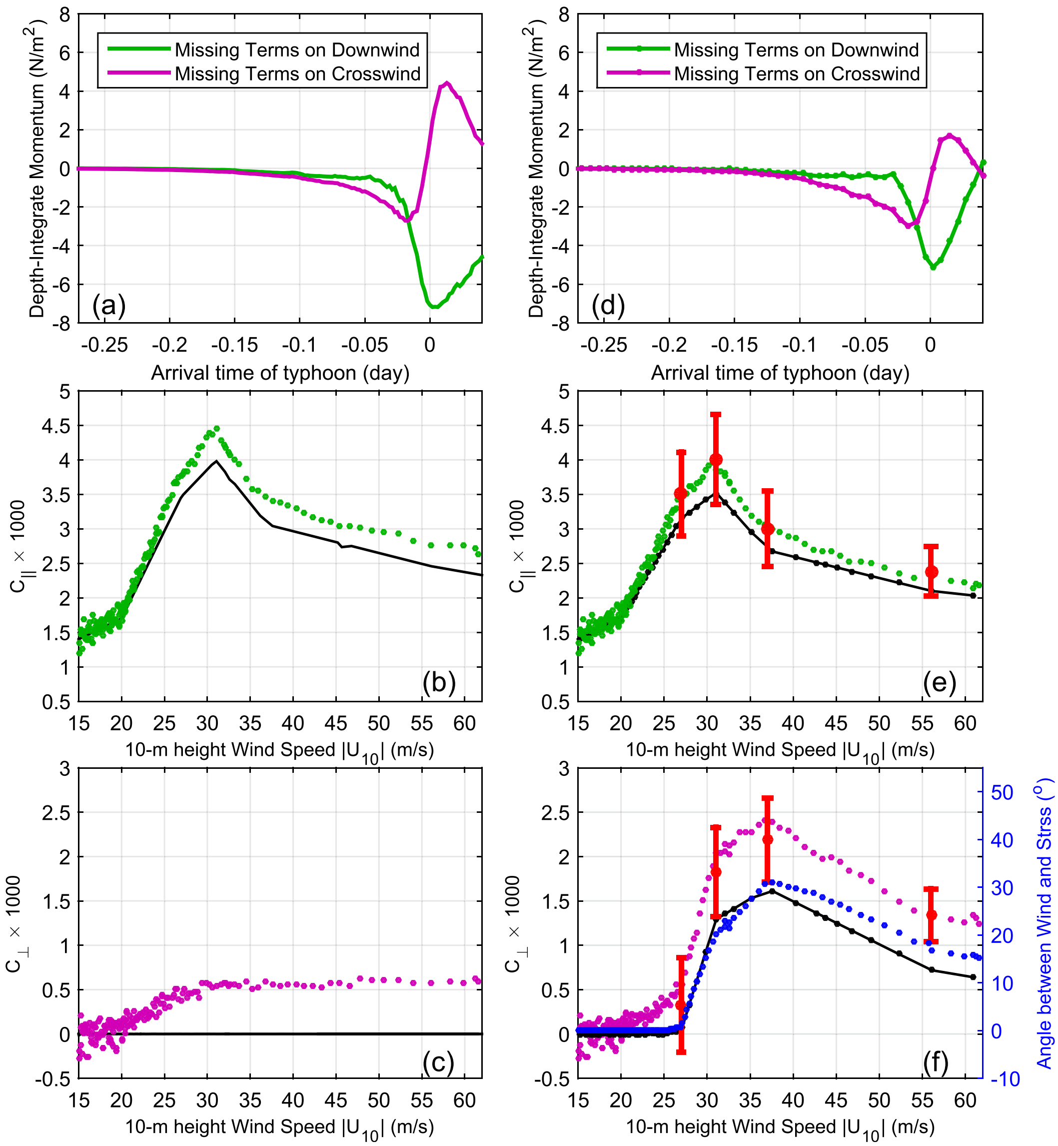

FIG. 6. Correction to the apparent drag coefficients due to nonlinear and pressure gradient terms in the momentum budget. (left) The results from the PWP3D model employing the apparent downwind drag coefficient obtained in this analysis: (a) the sum of the nonlinear and pressure gradient terms on the downwind (green) and crosswind (purple) directions, (b) the apparent downwind drag coefficient (black) and the drag coefficient derived assuming a linear momentum balance (green dots), and (c) the zero crosswind drag coefficient used in the PWP3D model (horizontal black line) and the crosswind drag coefficient derived assuming a linear momentum balance (purple dots). (right) The results from the PWP3D model employing the adjusted downwind and crosswind drag coefficients: (d) the sum of the nonlinear and pressure gradient terms on the downwind (green) and crosswind (purple) directions; (e) the adjusted downwind drag coefficient (black), the downwind drag coefficient computed from the linear momentum budget (green dots), and the observed apparent downwind drag coefficient (red dots and vertical bars); and (f) the adjusted downwind drag coefficient (black), the crosswind drag coefficient computed from the linear momentum budget (purple dots), and the observed apparent crosswind drag coefficient (red dots and vertical bars). The blue dots in (f) show the angle between the wind and stress computed in simulation B. These final results are replotted in Fig. 1.

et al. (2012). The discrepancy between simulated ocean momentum response in simulation B at 42 km to the right of Megi's track and observations (Fig. 7e) suggests that the drag coefficient may be affected by factors other than the wind speed.

8. Discussion

Many prior studies use wind speed profiles observed in the atmospheric boundary layer to investigate the neutral drag coefficient under tropical cyclones (Powell

TABLE 2. The mean and standard errors of adjusted downwind and crosswind drag coefficients at different wind speed intervals during Typhoon Megi. Same as the values shown in Fig. 1.

	Wind speed at 10 m above the sea surface, $\|\mathbf{U}_{10}\|$ (m s^{-1})			
Drag coefficient in Typhoon Megi	$\|\mathbf{U}_{10}\| = 27 \pm 2$	$\|\mathbf{U}_{10}\| = 31 \pm 3$	$\|\mathbf{U}_{10}\| = 37 \pm 3$	$\|\mathbf{U}_{10}\| = 56 \pm 9$
Downwind $C_{\parallel}$ ($\times$1000)	3.2 $\pm$ 0.6	3.5 $\pm$ 0.7	2.6 $\pm$ 0.5	2.0 $\pm$ 0.4
Crosswind $C_{\perp}$ ($\times$1000)	0 $\pm$ 0.5	1.3 $\pm$ 0.5	1.6 $\pm$ 0.5	0.7 $\pm$ 0.3

et al. 2003; Holthuijsen et al. 2012). In this study we instead use oceanic momentum response to study tropical cyclone surface wind stress (Jarosz et al. 2007; Sanford et al. 2011). The estimates of surface wind stress are parameterized by wind speed as drag coefficients.

For $|\mathbf{U}_{10}| < 30\,\mathrm{m\,s^{-1}}$, the drag coefficient increases with wind speed, in agreement with previous studies (Fig. 1a). For $|\mathbf{U}_{10}| = 30$–$40\,\mathrm{m\,s^{-1}}$, the magnitude of $C_{\parallel} > 3.0 \times 10^{-3}$ agrees with that reported in an atmosphere–wave–ocean coupled model at the front-right quadrant of tropical cyclones (Chen et al. 2013) but is much greater than the neutral drag coefficient reported by others (Powell et al. 2003; Donelan et al. 2004). The unstable planetary boundary layer and complex surface wave field under Typhoon Megi may have caused the high drag coefficient (Dyer 1974; Chen et al. 2013). For $|\mathbf{U}_{10}| > 40\,\mathrm{m\,s^{-1}}$, the drag coefficient decreases with wind speed, in agreement with other studies (Powell et al. 2003; Holthuijsen et al. 2012) that propose drag coefficient saturation by sea foam and spray (Powell et al. 2003; Donelan et al. 2004).

For the crosswind component of surface wind stress for $|\mathbf{U}_{10}| < 30\,\mathrm{m\,s^{-1}}$, the angle between wind and stress is nearly zero, indicating that the assumed alignment between wind and stress in Monin–Obukhov similarity theory is valid under Typhoon Megi at low wind speeds. For $|\mathbf{U}_{10}| > 30\,\mathrm{m\,s^{-1}}$, the angle between wind and stress vectors is >15° (Fig. 1b), slightly greater than a numerical model result from the front-right quadrant of tropical cyclones (Chen et al. 2013). Previous studies suggest swell traveling under the tropical cyclone may yield significant crosswind stress (Chen et al. 2013; Reichl et al. 2014; Potter et al. 2015). The $C_{\perp}$ decreases for $|\mathbf{U}_{10}| > 40\,\mathrm{m\,s^{-1}}$, similar to the dependence of $C_{\parallel}$ on wind speed.

9. Summary

Velocity, temperature, and salinity measurements were taken by seven EM-APEX floats air deployed on the right side of Typhoon Megi, a small and fast-moving category 5 typhoon, during the ITOP experiment in 2010. Downwind and crosswind drag coefficients were computed from three floats closest to the eye using the depth-integrated linear momentum equation.

Extensive efforts are devoted to estimate the uncertainty of the derived drag coefficients due to the uncertainty in velocity measurements and imperfections in removing non-wind-driven currents. Estimates of the "apparent" drag coefficients are made assuming a linear momentum equation. PWP3D model simulations show that the momentum balance is approximately linear before the arrival of the eye but with significant components of nonlinear and pressure gradient force after the passage of Megi. The effects of nonlinear and pressure gradient terms before the arrival of the typhoon are corrected using the model to obtain the adjusted downwind and crosswind drag coefficients (Fig. 1; Table 2).

At $|\mathbf{U}_{10}| = 27\,\mathrm{m\,s^{-1}}$, our estimates of the downwind drag coefficient $C_{\parallel} = 3.2 \pm 0.6 \times 10^{-3}$ are greater than the C_d reported in previous studies (Powell et al. 2003; Donelan et al. 2004; Black et al. 2007; Jarosz et al. 2007). At $|\mathbf{U}_{10}| = 31\,\mathrm{m\,s^{-1}}$, our estimates of the downwind drag coefficient $C_{\parallel} = 3.5 \pm 0.7 \times 10^{-3}$ are much greater than previously reported and a factor of 2 greater than the drag coefficient on the right side of tropical cyclones reported by Holthuijsen et al. (2012). Our results are in agreement with the numerical model study by Chen et al. (2013), which reports a stronger drag coefficient, $>3.0 \times 10^{-3}$, in the front-right quadrant of tropical cyclones. At higher wind speeds our estimates of $C_{\parallel}$ decrease to 2.0×10^{-3} at $|\mathbf{U}_{10}| = 50\,\mathrm{m\,s^{-1}}$ and remain nearly constant to our observed maximum wind speed of $62\,\mathrm{m\,s^{-1}}$, consistent with the C_d reported by Bell et al. (2012).

We present, for the first time, measurements of the crosswind drag coefficient $C_{\perp}$ as a function of $|\mathbf{U}_{10}|$ in tropical cyclones. For $|\mathbf{U}_{10}| \leq 25\,\mathrm{m\,s^{-1}}$, estimates of $C_{\perp}$ are $\pm 0.5 \times 10^{-3}$. At $|\mathbf{U}_{10}| = 27\,\mathrm{m\,s^{-1}}$, the wind stress vector is about 10° clockwise from the wind vector, consistent with the report by Zhang et al. (2009) for lower wind speeds. For $|\mathbf{U}_{10}| > 30\,\mathrm{m\,s^{-1}}$, $C_{\perp}$ increases to $>1.0 \times 10^{-3}$, and the wind stress vector is mostly >20° clockwise from the wind vector. Chen et al. (2013), in their atmosphere–wave–ocean model simulations, report a similar result near the center of a tropical cyclone. As the wind speed increases from 40 to $60\,\mathrm{m\,s^{-1}}$, $C_{\perp}$ decreases to 0.7×10^{-3}. The decrease of $C_{\perp}$ at higher wind speeds, say $>40\,\mathrm{m\,s^{-1}}$, is similar to the decrease in $C_{\parallel}$.

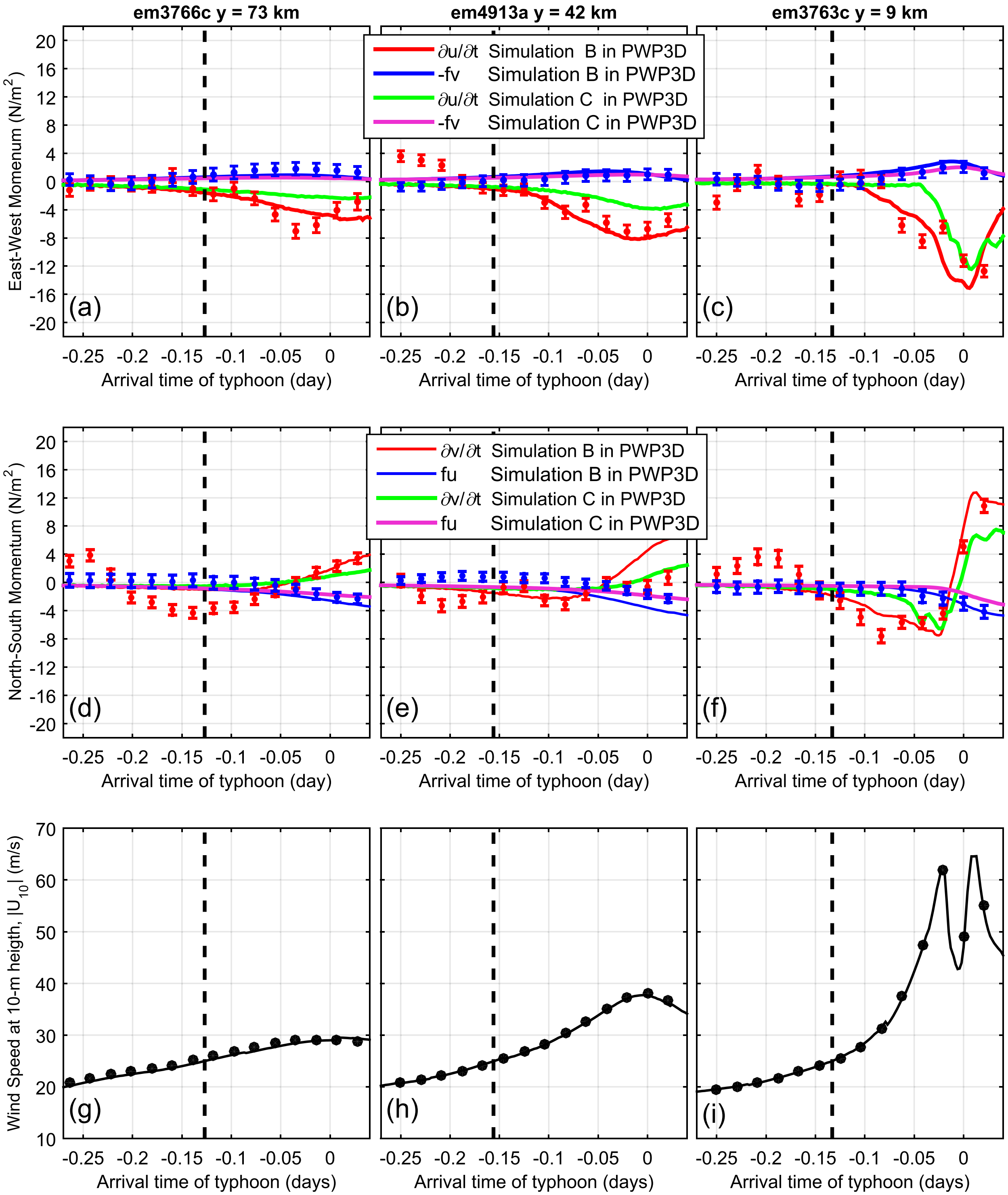

FIG. 7. Comparisons of float observations (dots with vertical error bars ± one standard deviation) and PWP3D model simulations of the depth-integrated (0–150 m) storm-induced (a)–(c) zonal linear momentum terms and (d)–(f) meridional linear momentum terms. Simulation B is performed using adjusted drag coefficients derived in the present analysis [red and blue curves in (a)–(f)]. Simulation C is performed using the C_d reported by Holthuijsen et al. (2012) [green and purple curves in (a)–(f)]. The observed wind speed at 10 m above the sea surface $|\mathbf{U}_{10}|$ at the floats' positions (black line with dots) is shown in the bottom panels. The abscissa is the time relative to the arrival time of Typhoon Megi's eye at the float array. The vertical dashed line represents the time when the measured wind speed at the float positions reaches 25 m s^{-1}.

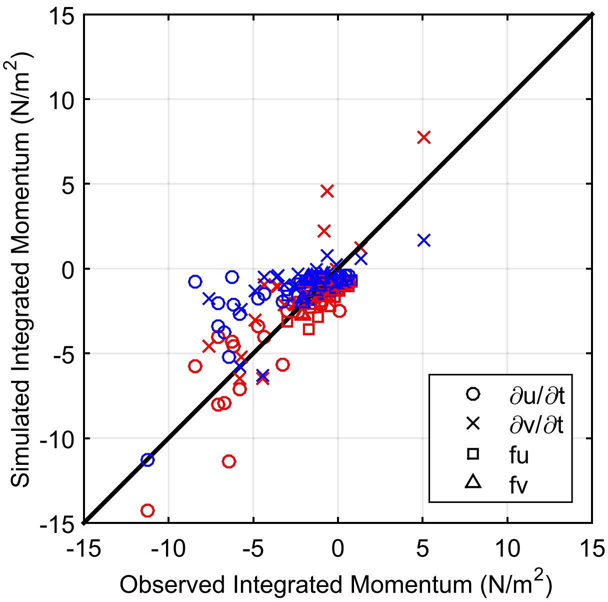

FIG. 8. Comparisons of float observations and model results of the depth-integrated (0–150 m), storm-induced, linear momentum terms [$\partial u/\partial t$ (circle), $\partial v/\partial t$ (cross), fu (square), and fv (triangle)] in simulation B (red) and simulation C (blue) before the passage of Typhoon Megi and at $|\mathbf{U}_{10}| > 25\,\mathrm{m\,s^{-1}}$.

This paper focuses on the drag coefficients under Typhoon Megi and on the details of the analysis method. Similar data are available for four other tropical cyclones (Hurricane Frances 2004, Hurricane Gustav 2008, Hurricane Ike 2008, and Typhoon Fanapi 2010). Drag coefficient analyses using the same method will be reported in a subsequent publication.

Acknowledgments. The authors appreciate the Office of Naval Research Physical Oceanography Program (N00014-08-1-0560, N00014-08-1-0577, N00014-10-1-0313, N00014-11-1-0375, and N00014-14-1-0360) for their support, the 53rd Weather Reconnaissance Squadron for their deployments of the EM-APEX floats, and J. F. Price for use of the PWP3D model. J. Carlson and J. Dunlap designed and built the EM sensor systems on the EM-APEX float. Constructive comments from J. F. Price and one anonymous reviewer are appreciated and greatly improved the presentation of this paper.

APPENDIX A

Typhoon Megi Wind Field

a. Wind speed processing

Continuous wind estimates at 10-m height above the sea surface $\mathbf{U}_{10}$ at each float were computed using data from aircraft penetrations of Typhoon Megi. Data from Vaisala RS92 dropsondes deployed by two WC-130J and one Taiwanese DOTSTAR aircraft (Wu et al. 2005) and from a nadir-looking SFMR (Uhlhorn and Black 2003) on the WC-130Js were used. These data can be obtained online (at http://catalog.eol.ucar.edu/itop_2010/). The positions of all measurements are determined by GPS data with an accuracy of better than 100 m.

The dropsondes measure horizontal wind velocity, temperature, and humidity from flight level to within a few meters above the sea surface. Wind speed accuracy is $\pm 0.5\,\mathrm{m\,s^{-1}}$ (UCAR/NCAR 1993). The $\mathbf{U}_{10}$ was computed directly from the RS92 dropsonde profiles.

The SFMR measures the brightness temperature, which is used to estimate surface wind speed continuously along the aircraft track with a nominal error of $4.0\,\mathrm{m\,s^{-1}}$ (Uhlhorn and Black 2003) for winds greater than $20\,\mathrm{m\,s^{-1}}$. The SFMR data were calibrated to the dropsonde 10-m winds using all SFMR and dropsonde data collected during ITOP. The SFMR measurement with only the highest quality data (Q2 = 4) was used to calibrate each nearby dropsonde measurement of $\mathbf{U}_{10}$. Measurement pairs separated by more than 18 s were rejected. A total of 343 pairs remained. Significant bias errors were found after comparing dropsonde and SFMR measurements at the same wind speed and were corrected using a cubic polynomial in $\log_{10}(|\mathbf{U}_{10}|)$. Corrections are small, $2\,\mathrm{m\,s^{-1}}$ or less for $|\mathbf{U}_{10}| = 20\text{–}50\,\mathrm{m\,s^{-1}}$, but rise rapidly below this. The SFMR winds below $20\,\mathrm{m\,s^{-1}}$ were discarded in this study. The corrected SFMR data matched the dropsonde data with an RMS error of $3.5\,\mathrm{m\,s^{-1}}$, less than the nominal SFMR error of $4.0\,\mathrm{m\,s^{-1}}$ (Uhlhorn and Black 2003) and much more than the dropsonde error of $0.5\,\mathrm{m\,s^{-1}}$. The differences showed no trends in time, with aircraft number, with the distance between the plane and the dropsonde, or with the logged quality of the data.

The corrected SFMR winds, regardless of logged quality, and the 10-m dropsonde winds were used to create maps of the $|\mathbf{U}_{10}|$ of Megi. Data from three aircraft surveys were used. Flight 530W deployed 16 dropsondes during two passes through the storm from ~0000 to 0400 UTC 16 October, immediately after deploying the EM-APEX floats. Flight 630W deployed 44 dropsondes during three passes through the storm from ~2100 UTC 16 October to ~0300 UTC 17 October. This was coordinated with a DOTSTAR flight that deployed 10 additional dropsondes around the periphery of the storm. The 744 data points (13 dropsondes) during this survey were within 100 km of the storm center at six different azimuths. This survey coincided with the passage of the storm's eye through the float array and is the

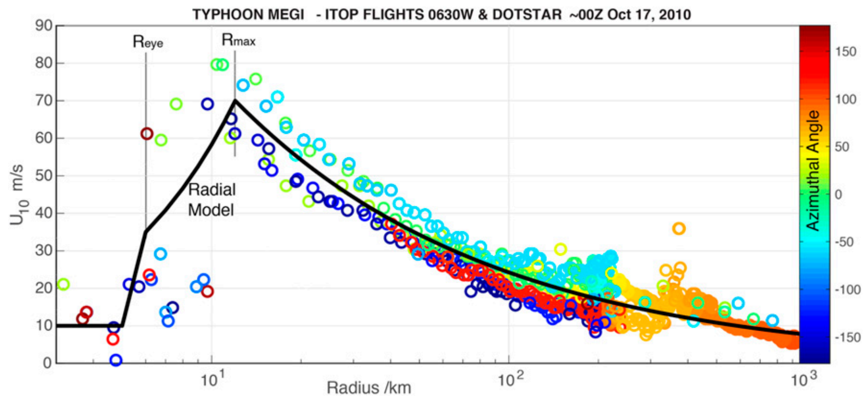

FIG. A1. Fit of radial model (black line) to all 10-m wind speed measurements from WC130 (630W) and DOTSTAR flights centered on 0000 UTC 17 Oct 2010. Color indicates the azimuthal angle of each measurement, clockwise from north.

primary source of data for the drag coefficient calculations. Flight 830W deployed 27 dropsondes during four passes through the storm from ~1100 to 1600 UTC 17 October.

For each survey, a continuous wind field was created in two steps. First, a radially symmetric wind field was fit to the observations. For radii $r > R_{\max}$ the form $V = (V_{\max}R_{\max}/r)^n$ was used. For $r < R_{\max}$, the form $V = V_{\max}(r/R_{\max})$ was used. Within the eye, $r < R_{\mathrm{eye}}$, and $V = V_{\mathrm{eye}}$. Figure A1 shows this function for the 17 October survey ($n = 0.5$, $R_{\max} = 12\,\mathrm{km}$, $V_{\max} = 70\,\mathrm{m\,s^{-1}}$, $R_{\mathrm{eye}} = 6\,\mathrm{km}$, and $V_{\mathrm{eye}} = 10\,\mathrm{m\,s^{-1}}$). Although this captures much of the wind variations, azimuthal deviations of up to $\pm 10\,\mathrm{m\,s^{-1}}$ are apparent. Both true azimuthal variations in the storm structure and errors in the location of the storm center used to make the radial map can cause the deviations. These deviations were then mapped (red regions in Fig. A2 representing a higher wind speed than the radial model and blue regions in Fig. A2 representing a lower wind speed) by smoothing the observations in polar coordinates using a Gaussian smoother with scales of 0.1 in $\log_{10}(r)$ and $\pi/4$ in azimuth and added to the radially symmetric model to form a wind field for the storm at the time of the survey. The standard deviation of the maps from the data is $1.8\,\mathrm{m\,s^{-1}}$ for Typhoon Megi, well within the expected uncertainty in the SFMR data. The deviations at the peak winds are $<1\,\mathrm{m\,s^{-1}}$. Two maps of the surface wind speed between the surveys, one earlier and one later, were constructed by moving the survey fields along the storm track, for example, the wind map of 17 October in Fig. A3. The $|\mathbf{U}_{10}|$ on the floats is computed by linearly interpolating these two maps in time.

The float positions are computed by linearly interpolating between roughly hourly GPS fixes, when these are available. Between approximately yeardays 289.4 and 291.5, the floats stopped surfacing to avoid damage and no GPS fixes are available. During these times, float positions were estimated by integrating the depth-averaged velocity measured by the floats, starting from the last GPS fix and adjusting this trajectory with a linear trend to hit the next GPS fix. The error is estimated from the size of this adjustment, typically a few centimeters per second, resulting in a position error of a few kilometers. The wind speeds computed at these floats' positions are used to calculate drag coefficient in this study (Fig. A4).

For the outer two floats, the lateral gradients are small. The uncertainty in the estimated wind speed is dominated by measurement and mapping errors. The former uncertainty is taken as the RMS SFMR error $\sim 3.5\,\mathrm{m\,s^{-1}}$, and the latter is conservatively taken as

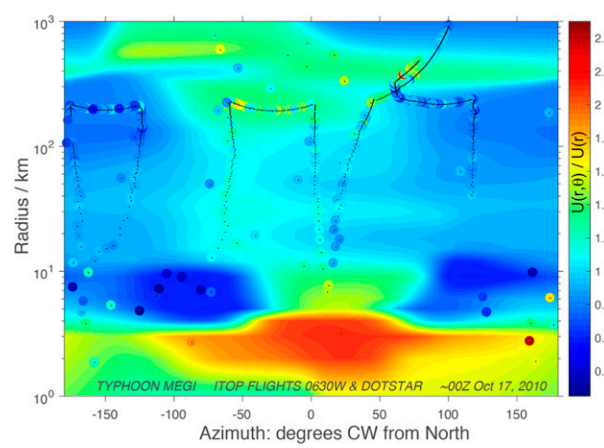

FIG. A2. Ratio of wind speed data (colored dots) to the radial model in Fig. 8 as a function of radius from the eye and azimuth from north. This is mapped to form a continuous function (colored).

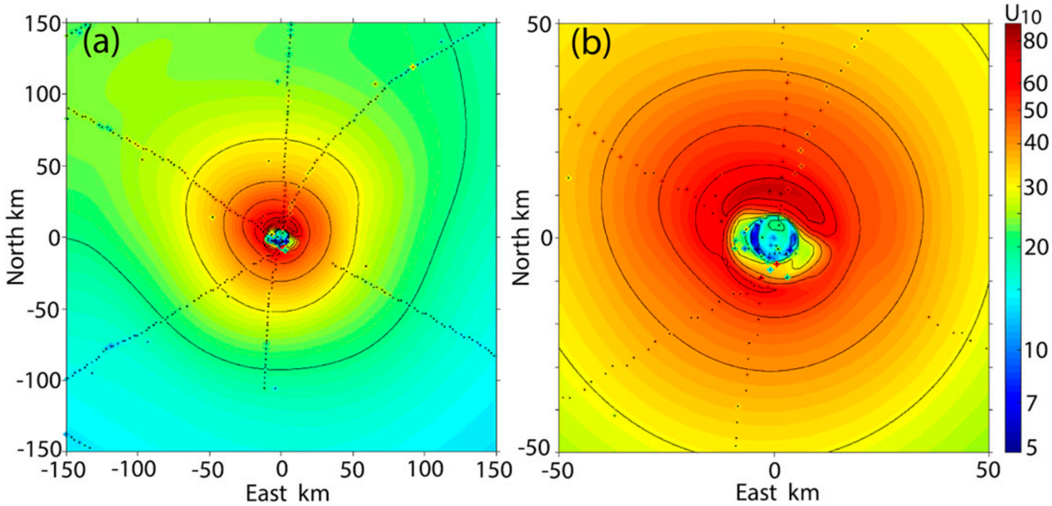

FIG. A3. Map of wind speed at 10-m height above the sea surface $|\mathbf{U}_{10}|$ (m s^{-1}) for 17 Oct 2010 aircraft surveys (630W) shown by background color with contours. Note logarithmic wind speed scale. Colored dots with black markers show measured wind speed. These are nearly invisible because they closely match the map. Map is shown at two different resolutions in the two panels.

the RMS deviation of the data from the map $\sim 1.8\,\mathrm{m\,s^{-1}}$. Combining these yields $4.0\,\mathrm{m\,s^{-1}}$ RMS. This error is conservative because much of the estimated SFMR error is undoubtedly due to variability in the dropsonde velocity estimates due to boundary layer turbulence.

The central float, under the greatest wind speed, passed under the storm eyewall north of the eye but inside the maximum wind region, one of high spatial gradients. The resulting time series of wind at the float is highly sensitive to the exact float track and the details of the wind map. In particular, the double wind peak results from the float passing under the comma-shaped wind maximum (Fig. A4). Neither the float track nor the wind map are sufficiently accurate to capture the details of this feature correctly. This large uncertainty only occurs for about 1 h while the float was in Megi's eyewall, with a plausible estimate of the RMS wind speed uncertainty at any given time $\pm 10\,\mathrm{m\,s^{-1}}$. The uncertainty in the peak hourly average wind speed is less because the float position is known to about 1 km from a recent GPS fix and the small advective velocities. Because the storm moved nearly westward, the float certainly went through the eyewall north of the eye in a region of 50–80 m s^{-1} winds. The average wind during this time is estimated at $71 \pm 5\,\mathrm{m\,s^{-1}}$ computed by fitting a smoothing spline to the nearby data points and resampling them randomly.

b. *Inflow angle of Typhoon Megi*

A basic description of the inflow angle of tropical cyclones is provided by the NOAA hurricane report (Schwerdt et al. 1979). Zhang and Uhlhorn (2012) studied the inflow angles of tropical cyclones using data taken from >1000 GPS dropsondes deployed in 18 tropical cyclones from 1998 to 2010. After removing the effect of storm motion on the cyclones' wind, the Cartesian wind vector is transformed to the tangential u_t and radial wind u_r components. The storm-relative inflow angle α is defined as

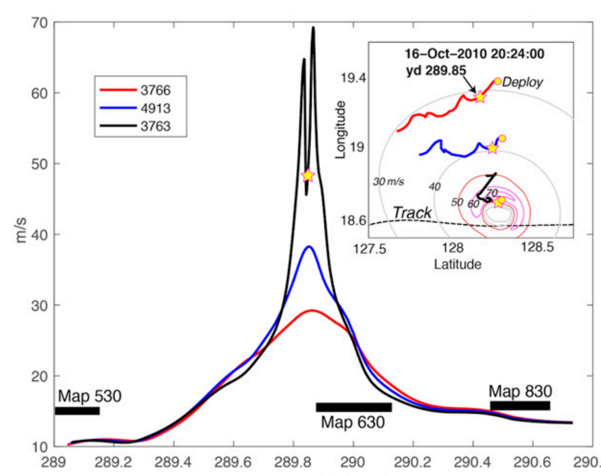

FIG. A4. Wind speed at three EM-APEX floats. Black bars show the times of the three storm surveys interpolated to the locations of each float. The inset shows contours of the mapped wind field at the time of peak wind at the innermost float. Heavy lines show the trajectories of the three floats each starting at a yellow circle and with the position of the yellow star at the time of the inset map. Dashed line shows the storm track moving from east to west.

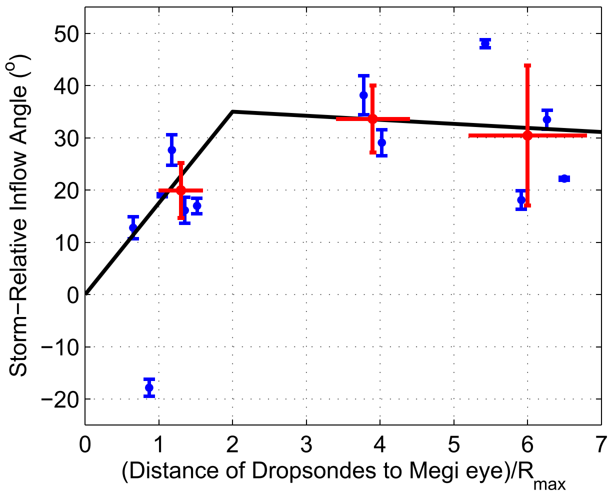

FIG. A5. The mean and standard deviation of storm-relative inflow angle averaged between 10 and 50 m above the sea surface $\overline{\alpha}$ at the front-right quadrant of Typhoon Megi (blue dots and vertical lines) measured from dropsondes. The dependence of inflow angle on the distance to Typhoon Megi's eye is normalized by the radius of maximum wind ($R_{\max}$). Mean inflow angle $\overline{\alpha}$ is bin averaged (red dots and error bars) in three bins of distance (horizontal red bars) corresponding to three EM-APEX floats' distance from Typhoon Megi's eye (em3763c, em4913a, and em3766c). The black solid line is the parameterization of storm-relative inflow angle as the function of distance to Typhoon Megi's eye used in this analysis.

$$\alpha = \tan^{-1}\left(-\frac{u_r}{u_t}\right).$$

The inflow angle α is positive when the air mass is transported inward to the eye of tropical cyclones.

Following Zhang and Uhlhorn (2012), we use data taken from GPS dropsondes deployed in Typhoon Megi between 0100 UTC 16 October and 1200 UTC 17 October to compute the inflow angle α. The mean of α ($\overline{\alpha}$), and standard deviation of α (σ_α) are computed within the layer between 10 and 50 m above the sea surface (blue dots and vertical lines in Fig. A5). The distance of each GPS dropsonde profile to the eye of Typhoon Megi is normalized by the radius of the storm's maximum wind ($R_{\max}$) as r^*. At the front-right quadrant of the storm beyond $R_{\max}$, that is, $r^* > 1$, the standard deviation σ_α is less than 5°.

We average $\overline{\alpha}$ within the front-right quadrant of the storm in three different bins of r^* corresponding to the distances of three EM-APEX floats nearest Typhoon Megi's eye. The average of $\overline{\alpha}$ is 20° ± 5° at $r^* = 1$–1.5, 32° ± 8° at $r^* = 3.4$–4.4, and 30° ± 13° at $r^* = 5.2$–6.8. Our results of $\overline{\alpha}$ within the front-right quadrant of Megi agree with those reported by Zhang and Uhlhorn (2012). In the present analysis, the storm-relative wind direction in Typhoon Megi is interpolated assuming α increases linearly from zero at Megi's eye to a peak value of 35° at $r^* = 2$ and decreases to 32° at $r^* = 6$. The effect of the storm motion is added to yield the interpolated vector wind field.

APPENDIX B

Estimates of Tides and Low-Frequency Ocean Currents on EM-APEX Floats

Tides and low-frequency currents can result in the surface wind stress induced by Typhoon Megi to fall out of balance with the integrated wind-driven momentum in the linear momentum budget. The following analysis focuses on the methods to estimate tidal and low-frequency currents and their corresponding uncertainties to isolate the current velocity for surface wind stress estimates. The subsurface mooring SA1, with an upward-looking 75-kHz ADCP mounted at 550-m depth, was located about 90 km west of the float array (Fig. 2b). The estimates of tides using the velocity measurements taken by the ADCP on the subsurface mooring SA1 are used to estimate tidal amplitude and phase at the EM-APEX floats positions.

a. Estimates of tidal amplitude and phase

We use harmonic fitting to estimate the phase and amplitude of the tides, assuming that the observed velocity is a linear superposition of mean current, inertial waves, and K_1 and M_2 tides. Velocity measurements on mooring SA1 show an amplitude of K_1 greater than O_1 and M_2 greater than S_2 (not shown in this study). The short time interval of velocity measurements on EM-APEX floats, ~3 days, is also not capable of separating the similar frequency signals for K_1 from O1 and S_2 from M_2.

The harmonic analysis is applied to EM-APEX float velocity measurements between 0200 UTC 16 October and 0100 UTC 19 October, with an inertial period at 18°–22°N of 32–38 h and a K_1 tidal period of 24 h and M_2 of 12.42 h. Note that the periods of inertial waves and diurnal tides are not far apart and therefore estimates of diurnal tides in the linear harmonic analysis could be biased by the presence of inertial waves induced by Megi. To minimize these contamination effects on the estimates of tidal currents, we apply the harmonic analysis to the velocity data between 200- and 220-m depth, which is much deeper than the penetration depth of the storm-induced inertial waves.

Table B1 summarizes tidal current amplitudes and phases estimated from velocity measurements taken from EM-APEX floats and on mooring SA1. The K_1 on SA1 leads the K_1 on the float (em4390d) at about 20.2°N

TABLE B1. The estimates of amplitude and phase of K_1 and M_2 tides from EM-APEX float and mooring SA1 observations. The tidal function is assumed as $A\cos(\omega t + \theta)$, where A is the amplitude, ω is the tidal frequency, and θ is the phase at $t = 0$, which is the arrival time of Typhoon Megi at the float array, about 2030 UTC 16 Oct. The subscripts x and y are the zonal and meridional directions, respectively. The harmonic fitting is applied to the velocity measurements between 200- and 220-m depth from 0200 UTC 16 Oct to 0100 UTC 19 Oct.

	Location		K_1 (diurnal tide)				M_2 (semidiurnal tide)			
Name	Lon (°E)	Lat (°N)	A_x (m s^{-1})	A_y (m s^{-1})	θ_x (°)	θ_y (°)	A_x (m s^{-1})	A_y (m s^{-1})	θ_x (°)	θ_y (°)
em3763c	128.2	18.7	0.12	0.15	137	−12.6	0.06	0.08	223.8	43.4
em4913a	128.2	19.0	0.14	0.12	195.4	39.9	0.04	0.05	170.6	−130.3
em3766c	128.1	19.3	0.11	0.12	188.2	27.6	0.07	0.12	99.5	−100.5
em4911a	128.1	19.6	0.13	0.12	165.6	0.2	0.08	0.11	109.4	−100.8
em4915a	128.1	19.8	0.11	0.10	177.9	13.0	0.05	0.07	117.5	−53.0
em4390d	128.2	20.2	0.15	0.14	169.5	3.6	0.03	0.08	193.4	10.6
Mooring	127.5	20.4	0.10	0.12	230.6	81.4	0.07	0.05	179.4	55.3
em4908a	128.2	20.8	0.12	0.12	155.8	−9.2	0.02	0.04	140.9	−74.4

by about 71° ± 9°. Assuming the K_1 tide propagates eastward from the Luzon Strait (Zhao 2014), we estimate a zonal wavelength of 310–400 km and a phase speed of 3.6–4.6 m s^{-1}. Our estimate of the phase speed agrees with the climatology K_1 phase speed from AVISO satellite observations of 4–5 m s^{-1} (Zhao 2014). Estimates of the M_2 tidal phase at the float array vary greatly, presumably due to multiple M_2 tide sources arriving on the experimental site, as suggested by Zhao (2014). The M_2 amplitude estimates from the floats are 0.04–0.14 m s^{-1} and are generally weaker than the K_1 tide.

b. Estimation of tides assuming first-mode baroclinic tide

We extrapolate tidal amplitude and phase estimated using EM-APEX float velocity measurements at 200–220-m depth to the layer above 200-m depth. The extrapolation depends on the vertical phase propagation and vertical structure of amplitude, which are not

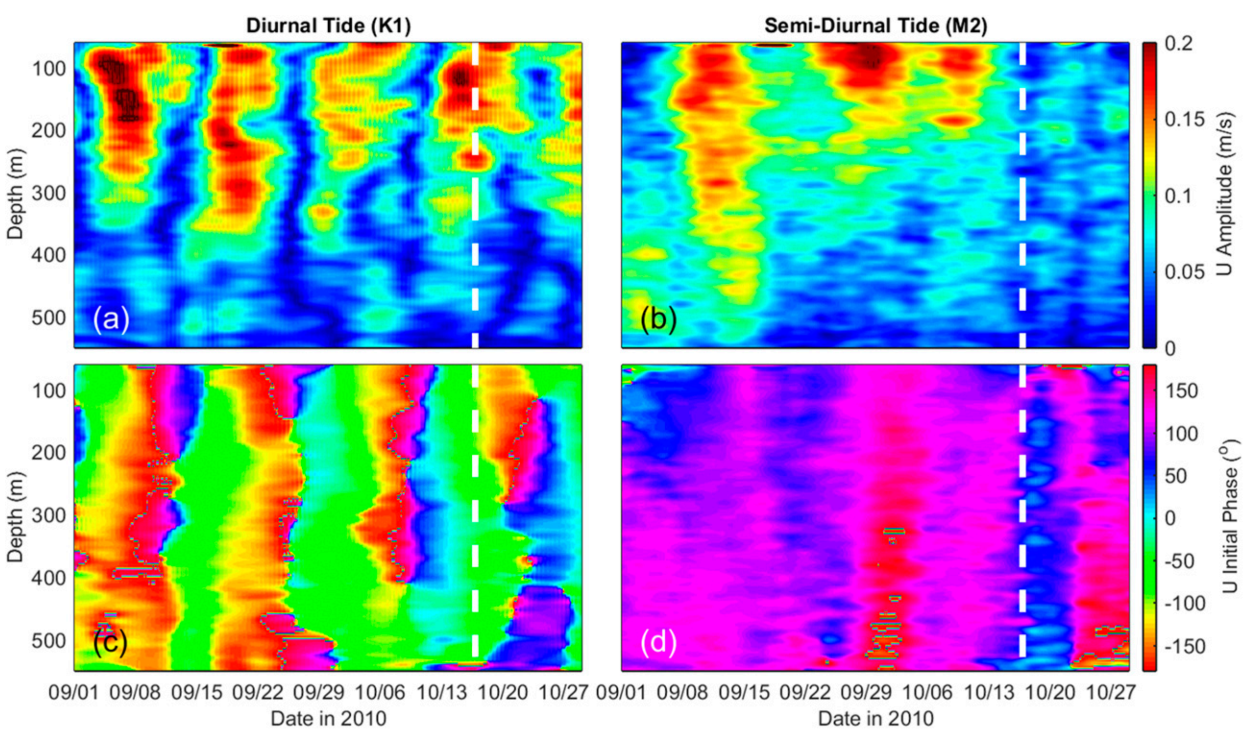

FIG. B1. Estimates of (top) amplitudes and (bottom) phases of (left) K_1 and (right) M_2 tidal zonal velocity at mooring SA1. A moving window of ±2 days is used in the harmonic analysis. The white dashed line shows the arrival time of the center of Typhoon Megi on the EM-APEX float array.

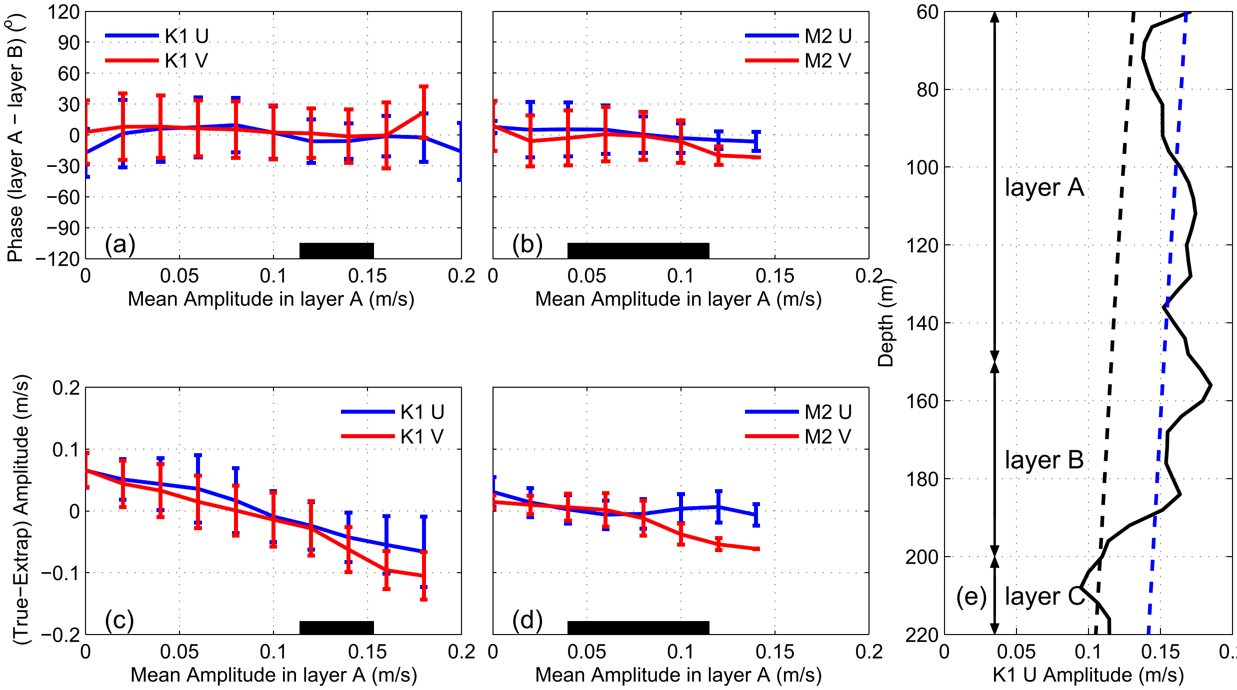

FIG. B2. Estimates of the vertical phase propagation and the error on the extrapolation of K_1 and M_2 amplitude from the deeper layer (layer C) on mooring SA1 to the upper layer using ADCP velocity from April to October 2010. (a),(b) The mean and one standard deviation of the difference of the estimated tidal phases between layers A and B, plotted as a function of tidal amplitude at 0.02 m s^{-1} interval. (c),(d) The mean and standard deviation of the difference of the estimated tidal amplitude in layer A from that extrapolated from layer C using the first baroclinic modal structure. The range of tidal amplitude estimated in layer C on EM-APEX floats is indicated as the thick black horizontal bars at the bottom of (a)–(d). (e) Example of the correction of tidal amplitude extrapolation on 0000 UTC 17 Oct at mooring SA1. The amplitude of the zonal velocity of the K_1 tide on the mooring (black thick line) in layer C is extrapolated to layer A based on the first-mode baroclinic tide vertical structure (black dashed line). The mean bias of amplitude between extrapolated and estimated tides within layer A is −0.03 m s^{-1} with the standard deviation 0.02 m s^{-1}.

available from limited float measurements. The vertical structure of tidal amplitudes and vertical phase propagation observed on mooring SA1 before Typhoon Megi (Fig. B1) are used to guide the vertical extrapolation of tidal amplitudes and phases on EM-APEX float positions.

We divide the velocity measurements on SA1 into three layers: (A) 60–150-m depth, (B) 150–200-m depth, and (C) 200–220-m depth. The phases of diurnal and semidiurnal tides estimated on SA1 do not show significant differences between layers A and B, with a mean phase difference of ~0 and a standard deviation of ~30°, and are independent of tidal amplitudes (Figs. B2a,b), suggesting a vertical standing feature of diurnal and semidiurnal tides.

We extrapolate the amplitude of tides on SA1 from layer C to layer A based on the vertical structure of the first-mode baroclinic tide. The eigenmode structure is obtained using the density profiles taken by Argo floats between the surface and 1600-m depth near SA1 and EM-APEX floats during 14–18 October. The difference between the tidal amplitude estimated directly from velocity in layer A and that estimated from the extrapolation from layer C is computed. Their mean values and one standard deviation of difference are computed as a function of the tidal amplitude in layer C. They vary from −0.08 to 0.05 m s^{-1} with one standard deviation about 0.03 m s^{-1} (Figs. B2c,d). The standard deviation of amplitude within layer A is 0.02 m s^{-1}. The amplitude difference due to extrapolation (Figs. B2c,d) is applied to the extrapolation of tidal amplitudes on EM-APEX float measurements.

c. *Estimation of low-frequency current*

Because the surface geostrophic current and the barotropic adjustment velocity $\overline{\mathbf{V}^*}$ in EM-APEX float velocity measurements have longer time scales than the near-inertial current, they are assumed as depth-dependent mean current during the EM-APEX float observational period. After removing the extrapolated tides, we average float velocity vertical profiles, from the earliest reliable and available velocity measurements at 0200 UTC 16 October to several hours (2, 3, 4, and 5 h) later, into one single profile as the mean current.

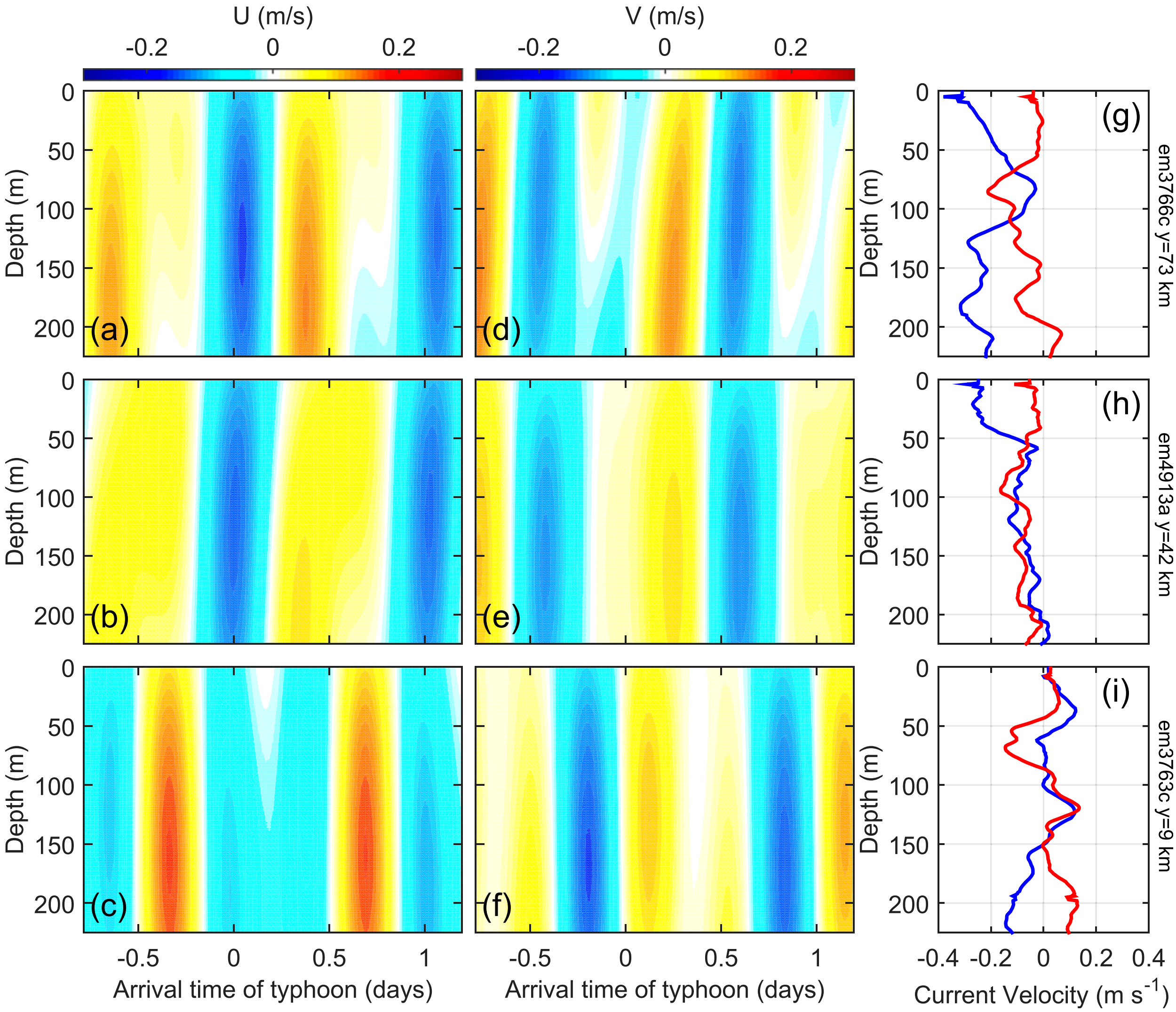

FIG. B3. (a)–(c) Average of tidal zonal current velocity, (d)–(f) tidal meridional current velocity, and (g)–(i) low-frequency zonal (blue lines) and meridional current (red lines) velocity in the stochastic simulation at three float positions (rows). Distances of floats from Megi's track are labeled to the right of the right column. Time is relative to the arrival of Typhoon Megi's eye at the float array.

d. *Tides and low-frequency current in the stochastic simulation*

The velocity of tides on the EM-APEX floats is extrapolated to the ocean surface assuming the vertical structure of the first-mode baroclinic tide; 10 000 simulations of normally distributed tides ($K_1 + M_2$) are generated in a stochastic simulation, using the mean and standard deviation of vertical phase propagation and amplitude difference according to the analysis of tides on mooring SA1 (appendix B, section b). The average velocity of tides near the ocean surface at the arrival of Typhoon Megi is ~0.1–0.15 m s^{-1} (Fig. B3). The low-frequency current is estimated in four different selected averaging periods (appendix B, section c) after removing the 10 000 simulations of tides. The average low-frequency current speed in the surface mixed layer is less than 0.1 m s^{-1} at the float em3763c on Typhoon Megi's track (Fig. B3). The 40 000 simulations of background current velocity (tides + low-frequency current) are removed from the EM-APEX velocity profiles before estimating surface wind stress.

REFERENCES

Bell, M. M., M. T. Montgomery, and K. A. Emanuel, 2012: Air–sea enthalpy and momentum exchange at major hurricane wind speeds observed during CBLAST. *J. Atmos. Sci.*, **69**, 3197–3222, doi:10.1175/JAS-D-11-0276.1.

Black, P. G., and Coauthors, 2007: Air–sea exchange in hurricanes: Synthesis of observations from the Coupled Boundary Layer

Air–Sea Transfer experiment. *Bull. Amer. Meteor. Soc.*, **88**, 357–374, doi:10.1175/BAMS-88-3-357.

Charnock, H., 1955: Wind stress on a water surface. *Quart. J. Roy. Meteor. Soc.*, **81**, 639–640, doi:10.1002/qj.49708135027.

Chen, S. S., W. Zhao, M. A. Donelan, and H. L. Tolman, 2013: Directional wind–wave coupling in fully coupled atmosphere–wave–ocean models: Results from CBLAST-Hurricane. *J. Atmos. Sci.*, **70**, 3198–3215, doi:10.1175/JAS-D-12-0157.1.

D'Asaro, E. A., and Coauthors, 2014: Impact of typhoons on the ocean in the Pacific. *Bull. Amer. Meteor. Soc.*, **95**, 1405–1418, doi:10.1175/BAMS-D-12-00104.1.

Donelan, M. A., B. K. Haus, N. Reul, W. J. Plant, M. Stiassnie, H. C. Graber, O. B. Brown, and E. S. Saltzman, 2004: On the limiting aerodynamic roughness of the ocean in very strong winds. *Geophys. Res. Lett.*, **31**, L18306, doi:10.1029/2004GL019460.

Drennan, W. M., H. C. Graber, and M. A. Donelan, 1999: Evidence for the effects of swell and unsteady winds on marine wind stress. *J. Phys. Oceanogr.*, **29**, 1853–1864, doi:10.1175/1520-0485(1999)029<1853:EFTEOS>2.0.CO;2.

——, ——, D. Hauser, and C. Quentin, 2003: On the wave age dependence of wind stress over pure wind seas. *J. Geophys. Res.*, **108**, 8062, doi:10.1029/2000JC000715.

Dyer, A. J., 1974: A review of flux-profile relationships. *Bound.-Layer Meteor.*, **7**, 363–372, doi:10.1007/BF00240838.

Edson, J. B., and Coauthors, 2013: On the exchange of momentum over the open ocean. *J. Phys. Oceanogr.*, **43**, 1589–1610, doi:10.1175/JPO-D-12-0173.1.

Emanuel, K. A., 1995: Sensitivity of tropical cyclones to surface exchange coefficients and a revised steady-state model incorporating eye dynamics. *J. Atmos. Sci.*, **52**, 3969–3976, doi:10.1175/1520-0469(1995)052<3969:SOTCTS>2.0.CO;2.

Geernaert, G. L., 1988: Measurements of the angle between the wind vector and wind stress vector in the surface layer over the North Sea. *J. Geophys. Res.*, **93**, 8215–8220, doi:10.1029/JC093iC07p08215.

Gill, A. E., 1984: On the behavior of internal waves in the wakes of storms. *J. Phys. Oceanogr.*, **14**, 1129–1151, doi:10.1175/1520-0485(1984)014<1129:OTBOIW>2.0.CO;2.

Grachev, A. A., C. W. Fairall, J. E. Hare, J. B. Edson, and S. D. Miller, 2003: Wind stress vector over ocean waves. *J. Phys. Oceanogr.*, **33**, 2408–2429, doi:10.1175/1520-0485(2003)033<2408:WSVOOW>2.0.CO;2.

Hock, T. F., and J. L. Franklin, 1999: The NCAR GPS dropwindsonde. *Bull. Amer. Meteor. Soc.*, **80**, 407–420, doi:10.1175/1520-0477(1999)080<0407:TNGD>2.0.CO;2.

Holthuijsen, L. H., M. D. Powell, and J. D. Pietrzak, 2012: Wind and waves in extreme hurricanes. *J. Geophys. Res.*, **117**, C09003, doi:10.1029/2012JC007983.

Jarosz, E., D. A. Mitchell, D. W. Wang, and W. J. Teague, 2007: Bottom-up determination of air-sea momentum exchange under a major tropical cyclone. *Science*, **315**, 1707–1709, doi:10.1126/science.1136466.

Johnson, H. K., J. Højstrup, H. J. Vested, and S. E. Larsen, 1998: On the dependence of sea surface roughness on wind waves. *J. Phys. Oceanogr.*, **28**, 1702–1716, doi:10.1175/1520-0485(1998)028<1702:OTDOSS>2.0.CO;2.

Large, W. G., and S. Pond, 1981: Open ocean momentum flux measurements in moderate to strong winds. *J. Phys. Oceanogr.*, **11**, 324–336, doi:10.1175/1520-0485(1981)011<0324:OOMFMI>2.0.CO;2.

Lien, R.-C., T. B. Sanford, S. Jan, M.-H. Chang, and B. B. Ma, 2013: Internal tides on the East China Sea continental slope. *J. Mar. Res.*, **71**, 151–185, doi:10.1357/002224013807343461.

Moon, I.-J., I. Ginis, and T. Hara, 2004: Effect of surface waves on air–sea momentum exchange. Part II: Behavior of drag coefficient under tropical cyclones. *J. Atmos. Sci.*, **61**, 2334–2348, doi:10.1175/1520-0469(2004)061<2334:EOSWOA>2.0.CO;2.

Potter, H., C. O. Collins, W. M. Drennan, and H. C. Graber, 2015: Observations of wind stress direction during Typhoon Chaba (2010). *Geophys. Res. Lett.*, **42**, 9898–9905, doi:10.1002/2015GL065173.

Powell, M. D., P. J. Vickery, and T. A. Reinhold, 2003: Reduced drag coefficient for high wind speeds in tropical cyclones. *Nature*, **422**, 279–283, doi:10.1038/nature01481.

Price, J. F., R. A. Weller, and R. Pinkel, 1986: Diurnal cycling: Observations and models of the upper ocean response to diurnal heating, cooling, and wind mixing. *J. Geophys. Res.*, **91**, 8411–8427, doi:10.1029/JC091iC07p08411.

——, T. B. Sanford, and G. Z. Forristall, 1994: Forced stage response to a moving hurricane. *J. Phys. Oceanogr.*, **24**, 233–260, doi:10.1175/1520-0485(1994)024<0233:FSRTAM>2.0.CO;2.

Reichl, B. G., T. Hara, and I. Ginis, 2014: Sea state dependence of the wind stress over the ocean under hurricane winds. *J. Geophys. Res. Oceans*, **119**, 30–51, doi:10.1002/2013JC009289.

Sanford, T. B., R. G. Drever, and J. H. Dunlap, 1978: A velocity profiler based on the principles of geomagnetic induction. *Deep-Sea Res.*, **25**, 183–210, doi:10.1016/0146-6291(78)90006-1.

——, J. H. Dunlap, J. A. Carlson, D. C. Webb, and J. B. Girton, 2005: Autonomous velocity and density profiler: EM-APEX. *Proc. IEEE/OES Eighth Working Conf. on Current Measurement Technology, 2005*, Southampton, United Kingdom, IEEE, 152–156, doi:10.1109/CCM.2005.1506361.

——, J. F. Price, and J. B. Girton, 2011: Upper-ocean response to Hurricane Frances (2004) observed by profiling EM-APEX floats. *J. Phys. Oceanogr.*, **41**, 1041–1056, doi:10.1175/2010JPO4313.1.

Schwerdt, R. W., F. P. Ho, and R. R. Watkins, 1979: Meteorological criteria for standard project hurricane and probable maximum hurricane wind fields, Gulf and east coasts of the United States. NOAA Tech. Rep. NWS 23, 320 pp. [Available online at https://docs.lib.noaa.gov/noaa_documents/NWS/TR_NWS/TR_NWS_23.pdf.]

Smith, S. D., 1980: Wind stress and heat flux over the ocean in gale force winds. *J. Phys. Oceanogr.*, **10**, 709–726, doi:10.1175/1520-0485(1980)010<0709:WSAHFO>2.0.CO;2.

UCAR/NCAR, 1993: NCAR Airborne Vertical Atmospheric Profiling System (AVAPS). UCAR/NCAR–Earth Observing Laboratory, accessed 30 October 2016, doi:10.5065/D66W9848.

Uhlhorn, E. W., and P. G. Black, 2003: Verification of remotely sensed sea surface winds in Hurricanes. *J. Atmos. Oceanic Technol.*, **20**, 99–116, doi:10.1175/1520-0426(2003)020<0099:VORSSS>2.0.CO;2.

Wang, H., and Y. Wang, 2014: A numerical study of Typhoon Megi (2010). Part I: Rapid intensification. *Mon. Wea. Rev.*, **142**, 29–48, doi:10.1175/MWR-D-13-00070.1.

Wu, C.-C., and Coauthors, 2005: Dropwindsonde Observations for Typhoon Surveillance near the Taiwan Region (DOTSTAR): An overview. *Bull. Amer. Meteor. Soc.*, **86**, 787–790, doi:10.1175/BAMS-86-6-787.

Zhang, F. W., W. M. Drennan, B. K. Haus, and H. C. Graber, 2009: On wind-wave-current interactions during the Shoaling Waves Experiment. *J. Geophys. Res.*, **114**, C01018, doi:10.1029/2008JC004998.

Zhang, J. A., and E. W. Uhlhorn, 2012: Hurricane sea surface inflow angle and an observation-based parametric model. *Mon. Wea. Rev.*, **140**, 3587–3605, doi:10.1175/MWR-D-11-00339.1.

Zhao, Z., 2014: Internal tide radiation from the Luzon Strait. *J. Geophys. Res. Oceans*, **119**, 5434–5448, doi:10.1002/2014JC010014.